

Bulletin of the Seismological Society of America

Vol. 68

June 1978

No. 3

THREE-DIMENSIONAL NUMERICAL SIMULATIONS OF DYNAMIC FAULTING IN A HALF-SPACE

BY RALPH J. ARCHULETA* AND GERALD A. FRAZIER†

ABSTRACT

A method is presented for the computation of near-field particle displacements and particle velocities resulting from a dynamic propagating, stress relaxation occurring on a finite fault plane embedded within a three-dimensional semi-infinite medium. To check our numerical procedure we compare our results for a circular fault in a full space with Kostrov's (1964) analytic solution for a self-similar propagating stress relaxation.

We have simulated two bilateral strike-slip earthquakes differing only in hypocentral location and examined the particle motion on the traction-free surface and on the rupture surface. Focusing of energy is evident in both ruptures. The static displacement on the rupture surface overshoots the theoretical static value by approximately 25 per cent. For the rupture that nucleated at depth the free surface almost doubled the particle velocities along the fault trace as compared with the rupture that nucleated at the free surface.

Our numerical results indicate that for an earthquake occurring on a semi-circular fault with radius of 10 km, an effective stress of 100 bars and a rupture velocity of 0.9β in a medium characterized by $\beta = 3$ km/sec, $\alpha = \sqrt{3}\beta$ and a density of 2.7 gm/cm³ particle velocities can reach 400 cm/sec and displacements 250 cm.

We also compare our numerical results with the observations made by Archuleta and Brune (1975) for a spontaneous stress relaxation on a semi-circular crack in a prestressed foam rubber block.

INTRODUCTION

The physical concept of elastic rebound as proposed by Reid (1910) is generally accepted as the mechanism for a tectonic earthquake. The essence of the elastic rebound hypothesis is that the tectonic stress in a region is relaxed as a shearing fracture (a discontinuity in the earth) spontaneously spreads over a finite zone (generally assumed to be a fault plane). Both the rate of growth and its geometry are a direct result of the stress state of the medium prior to rupture, the instantaneous stress state in the medium during rupture, and a fracture criterion determining whether or not the rupture front advances. The earth as the medium can be inhomogeneous and anisotropic. The earth is finite and has a stress-free surface which may be intersected by the fracture area. Although we have a qualitative description of an earthquake mechanism, there is no quantitative solution which totally embodies the premises of Reid's concept.

There are many valid approximations to the complete solution. Obtaining better

* Current Address: Office of Earthquake Studies, U.S. Geological Survey, 345 Middlefield Road, Menlo Park, California 94025.

† Current Address: Del Mar Technical Associates, P.O. Box 1083, Del Mar, California 92014.

approximations to the complete quantitative solution of earthquake dynamics not only enables one to appraise the physics of the source but also allows one to determine more accurately the expected near-field ground motion for engineering purposes. Kinematic models in which the discontinuity in displacement on the fault is specified *a priori* have been used by many researchers, e.g., Haskell (1964), Savage (1966), Aki (1968), Boore *et al.* (1971), Trifunac and Udawadia (1974) and Anderson and Richards (1975), to name but a few. In 1964 Kostrov derived the first three-dimensional analytical solution for a shear stress relaxation on a plane. However, Kostrov's solution required a continuously expanding fault plane in an infinite medium. This work was later extended by Burridge and Willis (1969), Richards (1973, 1976), and Burridge and Levy (1974). An analytical solution for a propagating stress relaxation on a finite fault in two dimensions was given by Burridge and Halliday (1971). Numerical solutions to two-dimensional fault dynamics have been presented by Burridge (1969), Hanson *et al.* (1974), and Cherry *et al.* (1976), and St öckl (1977). A three-dimensional numerical solution for a finite fault plane in a full space has been published by Madariaga (1976). Another finite fault in a full space has been analyzed by Bache *et al.* (1976). Using finite elements Dieterich (1973) examined a spontaneously propagating rupture. Other researchers have pursued an approach in which spontaneous fracture is a direct result of a fracture energy criterion (Griffith, 1921). The results to date have been two-dimensional, Kostrov (1966, 1974), Ida (1972), Eshelby (1969), Freund (1972), Hussein *et al.* (1975), Andrews (1976), Das and Aki (1977).

The above list is of course only a partial listing of the many researchers who have approximated a quantitative representation for the elastic rebound hypothesis. In this paper we shall present another approximation that extends some of the previous work by simulating an earthquake as a propagating stress relaxation over a finite fault area embedded within a semi-infinite medium that includes a stress-free surface. The fault plane may or may not intersect the stress-free surface. In this model we specify the initial stress, the coefficient of sliding friction, the rupture velocity, the geometry of the fault including the hypocenter, and the properties of the medium. This model is an approximation in that the rupture velocity and the fault geometry are specified *a priori*. However, the model is a fully three-dimensional, dynamic fracture occurring in a semi-infinite medium.

EARTHQUAKE MODEL

We will represent an earthquake as a propagating stress relaxation over a finite fault plane embedded within a half-space. The fault plane may or may not intersect the surface of the half-space. To implement this model we specify the hypocenter, the geometry of the fault plane, the rupture velocity, the initial stress in the medium, and the coefficient of sliding friction. Although portions of the following general formulation of the problem of a propagating stress relaxation have been presented elsewhere including a full description by Kostrov (1970), in order to be clear about our terminology and the approach that guided our numerics we present in this section the mathematical basis for a propagating stress relaxation in the presence of friction. Later in this section we specialize to the case of a strike-slip earthquake.

Figure 1 shows an arbitrarily oriented fracture surface embedded within a half-space. We will use a Cartesian coordinate system (determined by three orthonormal vectors $(\mathbf{x}_1, \mathbf{x}_2, \mathbf{x}_3)$). (The $\hat{\cdot}$ above any vector indicates that vector has unit length.) We denote by $\mathbf{u}(\mathbf{x}, t)$ the particle displacement vector at position \mathbf{x} and time t relative to its position at time $t = 0$. We denote by $\mathbf{S}(\mathbf{x}, t)$ the total stress tensor at

position \mathbf{x} and time t . The surface of the half-space with outward normal $\hat{\nu}(\mathbf{x})$ is traction-free

$$\mathbf{S}(\mathbf{x}, t) \cdot \hat{\nu}(\mathbf{x}) = 0. \tag{1}$$

The fault area at time t on which the slip velocity is nonzero is designated by $\Sigma(\mathbf{x}, t)$; the area of the final ruptured surface is designated by $\Sigma_0(\mathbf{x})$. The discontinuity in particle displacement (slip) on $\Sigma(\mathbf{x}, t)$ is denoted by $\mathbf{s}(\mathbf{x}, t)$ and defined for \mathbf{x} on $\Sigma(\mathbf{x}, t)$ as

$$\mathbf{s}(\mathbf{x}, t) = \lim_{\epsilon \rightarrow 0} [\mathbf{u}(\mathbf{x} - \epsilon \hat{\mathbf{n}}(\mathbf{x}), t) - \mathbf{u}(\mathbf{x} + \epsilon \hat{\mathbf{n}}(\mathbf{x}), t)] \tag{2}$$

where ϵ is a positive real number, and $\hat{\mathbf{n}}(\mathbf{x})$ is an outward normal to the plane $\Sigma(\mathbf{x}, t)$. The slip velocity is given by

$$\dot{\mathbf{s}}(\mathbf{x}, t) = \frac{\partial}{\partial t} \mathbf{s}(\mathbf{x}, t). \tag{3}$$

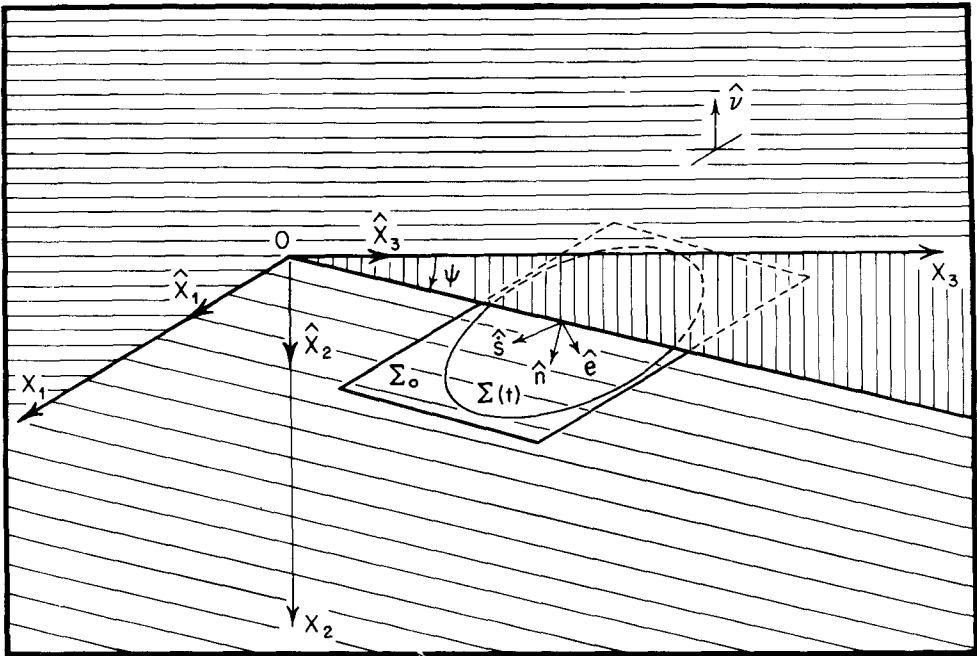


FIG. 1. A sketch of the geometry of a rupture surface $\Sigma(t)$ embedded within a half-space designated by basis vectors $\mathbf{x}_1, \mathbf{x}_2, \mathbf{x}_3$. Σ_0 is the final area of fracture; $\mathbf{n}, \hat{\mathbf{s}}, \mathbf{e}$ are unit vectors normal to $\Sigma(t)$, in the plane $\Sigma(t)$ and in the direction of instantaneous slip, in the plane $\Sigma(t)$ and perpendicular to $\hat{\mathbf{s}}$, respectively. The plane $\Sigma(t)$ has a dip ψ with respect to the traction-free surface whose outward normal is $\hat{\nu}$.

The final unit vector characterizing the rupture surface is

$$\hat{\mathbf{e}}(\mathbf{x}, t) = \hat{\mathbf{s}}(\mathbf{x}, t) \times \hat{\mathbf{n}}(\mathbf{x}). \tag{4}$$

For the remainder of this section the unit vectors $\hat{\mathbf{n}}(\mathbf{x}), \hat{\mathbf{s}}(\mathbf{x}, t)$ and $\hat{\mathbf{e}}(\mathbf{x}, t)$ will be written without their arguments.

We now consider the conditions that apply to $\Sigma(\mathbf{x}, t)$ in order to simulate sliding friction. First we require that the fracture mechanism be shear failure only by not allowing a discontinuity in particle displacement normal to $\Sigma(\mathbf{x}, t)$

$$\mathbf{s}(\mathbf{x}, t) \cdot \hat{\mathbf{n}} = 0. \quad (5)$$

The condition that on $\Sigma(\mathbf{x}, t)$ sliding friction opposes the slip velocity is given by

$$\hat{\mathbf{n}} \cdot \mathbf{S}(\mathbf{x}, t) \cdot \hat{\mathbf{s}} = -S_F(\mathbf{x}, t) \quad (6)$$

where $S_F(\mathbf{x}, t)$ is the magnitude of the traction due to sliding friction

$$S_F(\mathbf{x}, t) = -\gamma(\mathbf{x}) \hat{\mathbf{n}} \cdot \mathbf{S}(\mathbf{x}, t) \cdot \hat{\mathbf{n}} \quad (7)$$

where

$$\hat{\mathbf{n}} \cdot \mathbf{S}(\mathbf{x}, t) \cdot \hat{\mathbf{n}} \leq 0$$

with $\gamma(\mathbf{x}) \geq 0$ being the coefficient of sliding friction. The auxiliary condition imposed during sliding is

$$\hat{\mathbf{n}} \cdot \mathbf{S}(\mathbf{x}, t) \cdot \hat{\mathbf{e}} = 0. \quad (8)$$

In order to heal the fault we must determine the time at which the slip velocity tries to reverse direction. This time can be determined by posing a hypothetical problem at each time increment: Suppose we forced the sliding to stop at position \mathbf{x} and time t . Then \mathbf{x} would become part of the continuum and would have associated with it a stress tensor, say $\mathbf{S}'(\mathbf{x}, t)$. We let $\dot{\mathbf{s}}(\mathbf{x}, t)$ be the slip velocity if the sliding had been allowed to continue. Now if $\hat{\mathbf{n}} \cdot \mathbf{S}'(\mathbf{x}, t) \cdot \dot{\mathbf{s}}(\mathbf{x}, t)$ is less than $S_F(\mathbf{x})$, then $\Sigma(\mathbf{x}, t)$ heals at \mathbf{x} , i.e., $\dot{\mathbf{s}}(\mathbf{x}, t)$ is set to zero and $\mathbf{s}(\mathbf{x}, t)$ is held fixed for all subsequent time. If the criterion $\hat{\mathbf{n}} \cdot \mathbf{S}'(\mathbf{x}, t) \cdot \dot{\mathbf{s}}(\mathbf{x}, t) < S_F(\mathbf{x})$ is not met, then sliding is allowed to continue. We point out later in this section that for the computations to be presented in this paper an approximation to this general criterion was used.

Subject to the above boundary conditions the particle motion is determined by the conservation of linear momentum

$$\nabla \cdot \mathbf{S}(\mathbf{x}, t) + \mathbf{f}(\mathbf{x}) = \rho \ddot{\mathbf{u}}(\mathbf{x}, t) \quad (9)$$

where \mathbf{f} is a vector representing any body forces, e.g., gravity, in the medium, ρ is the density of the medium, and the pair of dots represent the second partial time derivative $\partial^2/\partial t^2$. The total stress tensor $\mathbf{S}(\mathbf{x}, t)$ ignoring effects due to rigid body rotations is a linear combination of the prestress tensor $\mathbf{S}^0(\mathbf{x})$ in the medium and the stress tensor $\boldsymbol{\sigma}(\mathbf{x}, t)$ that results from the fracture process

$$\mathbf{S}(\mathbf{x}, t) = \mathbf{S}^0(\mathbf{x}) + \boldsymbol{\sigma}(\mathbf{x}, t). \quad (10)$$

Since the prestress is in equilibrium with the body force

$$\nabla \cdot \mathbf{S}^0(\mathbf{x}) + \mathbf{f}(\mathbf{x}) = 0, \quad (11)$$

equation (9) reduces to

$$\nabla \cdot \boldsymbol{\sigma}(\mathbf{x}, t) = \rho \ddot{\mathbf{u}}(\mathbf{x}, t). \tag{12}$$

We further assume that everywhere outside of $\Sigma(\mathbf{x}, t)$ the medium is linearly elastic, isotropic, and homogeneous. Hence

$$\boldsymbol{\sigma}(\mathbf{x}, t) = 2\mu\boldsymbol{\epsilon}(\mathbf{x}, t) + \lambda(tr \boldsymbol{\epsilon})\mathbf{I} \tag{13}$$

where μ and λ are Lamé parameters, $\boldsymbol{\epsilon}(\mathbf{x}, t)$ is the strain tensor, \mathbf{I} is the identity tensor, and $tr \boldsymbol{\epsilon}$ is the trace of $\boldsymbol{\epsilon}(\mathbf{x}, t)$. The strain tensor $\boldsymbol{\epsilon}(\mathbf{x}, t)$ is related to the particle displacement by

$$\boldsymbol{\epsilon}(\mathbf{x}, t) = \frac{1}{2} (\nabla \mathbf{u}(\mathbf{x}, t) + [\nabla \mathbf{u}(\mathbf{x}, t)]^T) \tag{14}$$

where $[\nabla \mathbf{u}(\mathbf{x}, t)]^T$ means the transpose of the tensor $\nabla \mathbf{u}$.

As an illustration of this general model of an earthquake we will consider a strike-slip earthquake occurring on a vertical fault plane embedded within a homogeneous and isotropic half-space. The geometry for this example is shown in Figure 2. The prescribed final fractured plane Σ_0 (the area within the semicircle of radius r_0) lies in the plane $x_3 = 0$ with $-\hat{\mathbf{x}}_3$ as its outward normal (\mathbf{n}); the outward normal for the traction-free surface is $-\hat{\mathbf{x}}_2$. Relative to the basis vectors $\mathbf{x}_1, \mathbf{x}_2, \mathbf{x}_3$ we designate $S_{ij}(\mathbf{x}, t)$ as the ij component of the total stress tensor where $i = 1, 2, 3$ and $j = 1, 2, 3$.

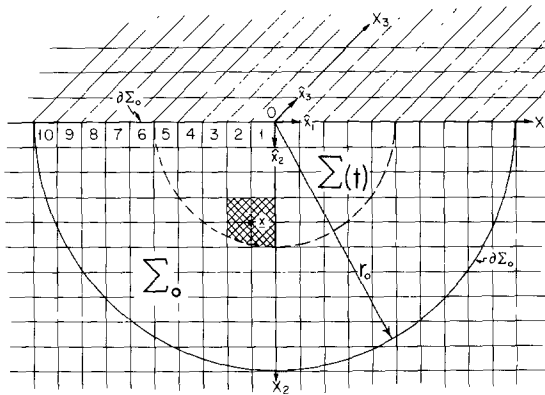


FIG. 2. Geometry of the fault surface used in the finite element computations for a strike-slip earthquake occurring on a semicircular, vertical fault plane.

Because we are considering a vertical fault plane within a homogeneous and isotropic half-space, the displacement field has symmetry properties with respect to the plane $x_3 = 0$, Haskell (1969)

$$u_1(x_1, x_2, 0^+, t) = -u_1(x_1, x_2, 0^-, t), \tag{15a}$$

$$u_2(x_1, x_2, 0^+, t) = -u_2(x_1, x_2, 0^-, t), \tag{15b}$$

$$u_3(x_1, x_2, 0^+, t) = u_3(x_1, x_2, 0^-, t), \tag{15c}$$

where $0^+(0^-)$ refers to the positive (negative) x_3 side of the plane.

We will examine the time evolution of the conditions for a particular particle located within Σ_0 at a point $\mathbf{P} = (x_1, x_2, 0^+)$. We divide this evolution into four periods: (1) the time preceding the nucleation of the rupture, $t < 0$; (2) the time between nucleation and the time (t_A) that the rupture front arrives at \mathbf{P} , $0 \leq t < t_A$; (3) the time after the arrival of the rupture front and the time (t_H) before the sliding stops at \mathbf{P} , $t_A \leq t < t_H$; (4) and finally the time after sliding has stopped, $t \geq t_H$. It should be noted that only in the time interval $t_A \leq t < t_H$ are boundary conditions applicable to the particle at \mathbf{P} , for it is only during that period that the particle at \mathbf{P} is a part of the surface $\Sigma(\mathbf{x}, t)$.

For this example we let the hypocenter be $(0, 0, 0)$ and let the rupture front expand at a constant velocity \mathbf{v} which is less than the shear-wave speed of the medium. Prior to nucleation, $t < 0$, the conditions at \mathbf{P} are

$$S_{ij}(\mathbf{P}, t) = S_{ij}^0(\mathbf{P}), \tag{16a}$$

$$\mathbf{u}(\mathbf{P}, t) = 0 \quad \text{and} \quad \dot{\mathbf{u}}(\mathbf{P}, t) = 0. \tag{16b}$$

For time t such that $0 \leq t < t_A$ the condition at \mathbf{P} is

$$S_{ij}(\mathbf{P}, t) = S_{ij}^0(\mathbf{P}) + \sigma_{ij}(\mathbf{P}, t) \tag{17a}$$

with

$$u_1(\mathbf{P}, t) = 0 \tag{17b}$$

and

$$u_2(\mathbf{P}, t) = 0 \tag{17c}$$

by the symmetry conditions, equations (15); $u_3(\mathbf{P}, t)$ is determined by the conservation of linear momentum. The stress $\sigma_{ij}(\mathbf{P}, t)$ is a result of fracture occurring on other parts of the fault. The perturbation in the stress field due to fracture propagates with the P -wave and S -wave speeds of the medium. Hence, this radiation arrives prior to the rupture front.

At a time t such that $t_A \leq t < t_H$ we apply the following boundary conditions

$$\mathbf{s}(\mathbf{P}, t) \cdot (-\hat{\mathbf{x}}_3) = 0, \tag{18a}$$

$$S_{31}(\mathbf{P}, t) = -S_F(\mathbf{P}) \cos \theta, \tag{18b}$$

and

$$S_{32}(\mathbf{P}, t) = -S_F(\mathbf{P}) \sin \theta \tag{18c}$$

where $\tan \theta = \dot{s}_2(\mathbf{P}, t) / \dot{s}_1(\mathbf{P}, t)$ and $S_F(\mathbf{P}) = \gamma(\mathbf{P})S_{33}^0(\mathbf{P})$. Because S_{33} is continuous across the plane $x_3 = 0$ and σ_{33} is an odd function with respect to x_3 for a vertical fault plane, $\sigma_{33}(x_1, x_2, 0, t) = 0$. Thus, $S_F(\mathbf{x}) = \gamma(\mathbf{x})S_{33}^0(\mathbf{x})$.

At the time t_H the quantity $[(S_{31}(\mathbf{P}, t_H))^2 + (S_{32}(\mathbf{P}, t_H))^2]^{1/2}$ is less than $S_F(\mathbf{P})$, and the rupture surface heals at \mathbf{P} . For all time $t \geq t_H$ the slip velocity $\dot{\mathbf{s}}(\mathbf{P}, t)$ is set to

zero and the slip $\mathbf{s}(\mathbf{P}, t)$ is fixed at the value it had just prior to the time t_H . Thus, permanent displacements are set within the medium.

A parameter that we will use to scale our results is the magnitude of effective stress $|\sigma_E(\mathbf{x}, t)|$. Actually, $\sigma_E(\mathbf{x}, t)$ is a traction, and for the general fault shown in Figure 1 is defined as

$$\sigma_E(\mathbf{x}, t) = \mathbf{T}^0(\mathbf{x}) - S_F(\mathbf{x})\hat{\mathbf{s}}(\mathbf{x}, t) \tag{19}$$

where

$$\mathbf{T}^0(\mathbf{x}) = \hat{\mathbf{n}} \cdot \mathbf{S}^0(\mathbf{x}) - (\hat{\mathbf{n}} \cdot \mathbf{S}^0(\mathbf{x}) \cdot \hat{\mathbf{n}})\hat{\mathbf{n}} \tag{20}$$

and $S_F(\mathbf{x}, t)$ is given by equation (7). The vector $\mathbf{T}^0(\mathbf{x})$ by definition has no component in the direction normal to the plane $\Sigma(\mathbf{x}, t)$ thereby ensuring that the fracture process relieves only the shear stress acting on $\Sigma(\mathbf{x}, t)$. The magnitude of $\sigma_E(\mathbf{x}, t)$ is

$$|\sigma_E(\mathbf{x}, t)| = \{\mathbf{T}^0(\mathbf{x}) \cdot \mathbf{T}^0(\mathbf{x}) - 2S_F\hat{\mathbf{n}} \cdot \mathbf{S}^0 \cdot \hat{\mathbf{s}} + S_F^2\}^{\frac{1}{2}} \tag{21}$$

In the particular example of a strike-slip earthquake occurring on a vertical fault plane

$$|\sigma_E(\mathbf{x}, t)| = \{[S_{31}^0(\mathbf{x})]^2 + [S_{32}^0(\mathbf{x})]^2 + S_F^2(\mathbf{x}) - 2S_F(\mathbf{x})[S_{31}^0(\mathbf{x}) \cos \theta + S_{32}^0(\mathbf{x}) \sin \theta]\}^{\frac{1}{2}} \tag{22}$$

where $\tan \theta = \dot{s}_2(\mathbf{x}, t)/\dot{s}_1(\mathbf{x}, t)$. We can further simplify this expression by assuming $S_{32}^0 = 0$ and replacing $S_F(\mathbf{x})$ by $-\gamma(\mathbf{x}) S_{33}^0(\mathbf{x})$

$$|\sigma_E(\mathbf{x}, t)| = \{[S_{31}^0(\mathbf{x})]^2 + [-\gamma(\mathbf{x})S_{33}^0(\mathbf{x})]^2 + 2\gamma(\mathbf{x})S_{33}^0(\mathbf{x})S_{31}^0(\mathbf{x}) \cos \theta\}^{\frac{1}{2}} \tag{23}$$

We see that if the friction vector is constrained to oppose only the motion in the $\hat{\mathbf{x}}_1$ direction, i.e., $\theta = 0$, then equation (23) is further reduced to

$$|\sigma_E(\mathbf{x}, t)| = S_{31}^0(\mathbf{x}) + \gamma(\mathbf{x})S_{33}^0(\mathbf{x}). \tag{24}$$

For the results in this paper we have assumed that $\theta = 0$, $S_{32}^0 = 0$, and have taken $|\sigma_E(\mathbf{x}, t)|$ to be a constant over the zone of rupture, $|\sigma_E(\mathbf{x}, t)| = \sigma_E$. Equation (24) allows numerous possibilities for the functions $S_{31}^0(\mathbf{x})$, $\gamma(\mathbf{x})$, $S_{33}^0(\mathbf{x})$ that could combine to form a constant σ_E . For example, suppose $S_{33}^0(\mathbf{x}) = -\rho g x_2$ where g is the acceleration due to gravity at the surface of the Earth, then two simple possibilities exist for $S_{31}^0(\mathbf{x})$ and $\gamma(\mathbf{x})$. First $\gamma(\mathbf{x})$ could be a constant, say γ , and $S_{31}^0(\mathbf{x}) = \sigma_E + \gamma\rho g x_2$; or secondly, $S_{31}^0(\mathbf{x})$ could equal $\sigma_E + 1$ while $\gamma(\mathbf{x}) = 1/(\rho g x_2)$. Another simple possibility is that $\gamma(\mathbf{x}) = 0$ with $S_{31}^0(\mathbf{x}) = \sigma_E$, i.e., complete stress relaxation. However, the last possibility leads to a problem of understanding what physical mechanism would prevent the fault from sliding, during the healing phase, opposite to the direction of the initial prestress. Regardless of what functions are chosen for

$S_{31}^0(\mathbf{x})$, $\gamma(\mathbf{x})$ and $S_{33}^0(\mathbf{x})$ to satisfy $|\sigma_E(\mathbf{x})| = \sigma_E$, the magnitude of the seismic radiation can be scaled by σ_E .

Because of our assumption for this paper that friction opposes only that motion in the $\hat{\mathbf{x}}_1$ direction, we used as our stopping criterion that the fault heals at \mathbf{x} when $u_1(\mathbf{x}, t)$ tries to reverse its direction. This simplified criterion does not seriously affect the time at which the fault heals but it does lead to a high-frequency spike in the $\hat{\mathbf{x}}_2$ component of particle velocity as can be seen in some later figures.

SCALING

Using the physical quantities— α , the P -wave speed; μ , the shear modulus; r_0 , the final fault radius; and σ_E , the magnitude of effective stress—we have cast all physical variables into dimensionless form (Madariaga, 1976)

$$\begin{aligned} \text{Length, } l &= r_0 \tilde{l} \\ \text{Time, } t &= r_0 / \alpha \tilde{t} \\ \text{Stress, } \sigma_{ij} &= \sigma_E \tilde{\sigma}_{ij} \\ \text{Displacement, } u_i &= r_0 \sigma_E / \mu \tilde{u}_i \\ \text{Particle Velocity, } u_i &= \alpha \sigma_E / \mu \tilde{u}_i, \end{aligned}$$

where the dimensionless parameters are designated by a tilde. All other variables that we will use can be derived from the above. In this presentation we have assumed our medium to be a Poisson solid, $\alpha = \sqrt{3}\beta$.

All the figures related to particle motion in this paper will be plotted in nondimensional quantities. Whenever we transform the nondimensional quantities to dimensional values, we shall assume the following numerical values: $\alpha = 5.196$ km/sec, $\beta = 3.0$ km/sec, $\mu = 2.43 \times 10^5$ bars, $r_0 = 10$ km, $\sigma_E = 100$ bars. Rather than repeat these values, we shall refer to them as the standard set of parameters for the medium and the fault. While these values approximate a class of earthquake conditions, other values can be employed to scale the dimensionless result for other particular situations with the restriction that $\alpha = \sqrt{3}\beta$.

FINITE ELEMENT TREATMENT

The continuum equations presented in the previous section are treated numerically using a finite element procedure originally described by Frazier and Petersen (1974). The displacement field is approximated over the interior of 8-node brick elements by linear interpolation to yield spatially discrete equations

$$[K]\{u(t)\} + [C]\{\dot{u}(t)\} + [M]\{\ddot{u}(t)\} = \{F(t)\} \quad (25)$$

where $\{u\}$ is a column listing of the three components of displacement at the N node points in the finite element grid. $[K]$ is a $3N$ by $3N$ stiffness matrix whose bending and torsional properties have been modified from strictly linear interpolation by the inclusion of incompatible (quadratic) deformation mode, i.e., the stiffness of each element is explicitly assigned according to beam theory. The viscosity matrix $[C]$, which is taken as proportional to $[K]$, serves to suppress spurious high-frequency signals that result from numerical dispersion. $[M]$ is a diagonal matrix which contains the effective mass that acts at each node in the finite element grid. Boundary conditions on the rupture surface Σ enter the numerical equations through the forcing matrix $\{F(t)\}$ as described in Appendix I.

An explicit method is used for integrating nodal displacements in time. Time-centered differencing is used for relating nodal accelerations $\{\ddot{u}(t)\}$ with nodal displacements

$$\Delta t^2 \{\ddot{u}(t)\} \cong \{u(t + \Delta t)\} - 2\{u(t)\} + \{u(t - \Delta t)\} \tag{26}$$

and backward differencing is used for relating the nodal velocities in the viscosity terms to nodal displacements

$$\Delta t \{\dot{u}(t)\} = \{u(t)\} - \{u(t - \Delta t)\} \tag{27}$$

where Δt is the numerical time increment. These temporally discrete forms are substituted into the equation (25) to provide our explicit equations for nodal displacements at the advanced time $t + \Delta t$

$$\begin{aligned} \{u(t + \Delta t)\} = & 2\{u(t)\} - \{u(t - \Delta t)\} + \Delta t^2 [M]^{-1} \{F(t)\} \\ & - \Delta t^2 [M]^{-1} [K] \{(1 + \Delta t d)u(t) - \Delta t d u(t - \Delta t)\} \end{aligned} \tag{28}$$

with $[C] = \Delta t d [K]$, d being a dimensionless damping coefficient.

To accommodate the rather massive grid involved in three-dimensional earthquake modeling, the stiffness matrix $[K]$ is not stored, but rather material properties and nodal positions are used to produce the matrix products $[K]\{u(t)\}$ at each time step. In this regard, our computing algorithm resembles finite difference procedures. Also, two damping coefficients d_p and d_s are used in the computer program to attenuate independently P waves and S waves.

Before numerically determining particle displacement, velocity, or acceleration we must understand how the numerical method provides an approximate solution to the differential equation. The basis of numerical techniques is discretization. The independent variables such as time, space, or both are discretized. Discretization results in an inherent limitation on the information obtained numerically. In a very real sense, discretization acts like a low-pass filter which when applied to the exact solution produces an approximate solution—the numerical one. The numerical solution cannot contain information for frequencies greater than the Nyquist frequency, $N_f = \frac{1}{2}\Delta t$.

We consider the finite element method as applied to simulating an earthquake. The important factor is discretization of the spacial continuum into finite elements, e.g., cubical volumes. The vertices of the elements are the points in space at which we will describe the particle motion. However, the computed particle motion is not the motion of a single point. The computed particle motion represents an average motion of the continuum within a grid dimension surrounding that point.

Analysis of the numerical equations and experience obtained from comparing numerical solutions with analytical solutions indicate that wavelengths greater than six grid dimensions ($6\Delta x$) are accurately synthesized, Smith (1974), Day (1977). A wavelength of six grid dimensions propagates slower than in a continuum by no more than 4 per cent. The amplitude of a six-grid-dimension wave decays with distance x excluding geometrical spreading by the factor $e^{-.04x/\Delta x}$ for calculations presented in this paper. The decay in amplitude with distance can be eliminated by prescribing $d = 0$; however, numerical dispersion then causes high frequency oscillations which can adversely affect the treatment of boundary conditions on the

rupture surface Σ .

Since the numerical method involves computer storage and costs, we do not have unlicensed freedom in choosing a grid. If we divide a given volume into elements, and then later divide that same volume into twice as many elements, the computer storage will be approximately eight times greater and the cost will be approximately sixteen times greater. (The numerical simulation of an earthquake involving 6000 three-dimensional elements averaged in time about 8 min. The numerical simulations were executed on a Control Data Corp. 7600 at Lawrence Berkeley Laboratory, Berkeley, California.)

This entire discussion is meant to emphasize an important feature of the finite element method: the particle motion is dependent on grid size. This dependence does not invalidate the results so long as one understands that the computed particle motion reflects an average motion of the continuum over a spatial domain characterized by the grid.

SELF-SIMILAR COMPARISON

In order to validate our finite element technique, we sought to compare our numerical results against a known three-dimensional, analytical solution for a propagating stress drop over a planar area. Thus we simulated Kostrov's (1964) self-similar problem of a rupture initiating at a point and then expanding with a constant speed as a circle over a plane in a full space. Referring to the geometry shown in Figure 2 the analytical solution for the \hat{x}_1 component of displacement at any point $(x_1, 0, 0^+)$ (where 0^+ refers to the positive \hat{x}_3 side of the fault) is

$$u_1 = c(v/\beta) \frac{\sigma_E}{\mu} \beta \sqrt{t^2 - x_1^2/v^2} H(t - x_1/v), \quad (29)$$

$c(v/\beta)$ is some constant computed by Dahlen (1974), v is the rupture speed, β is the S -wave speed, and $H(t)$ is the Heaviside step function. In our numerical simulation, we limited the size of the fault to a radius r_0 . However, until any effects due to the finiteness of the fault propagate to an observer, the self-similar solution should remain valid. For this particular example, we have taken a rupture velocity such that

$$v = 0.9\beta. \quad (30)$$

Symmetry considerations of the displacement field allow us to simulate numerically this problem using one octant of a full space. Symmetry properties permit us to consider only the positive x_3 space. The rupture is symmetric with respect to the plane $x_1 = 0$; thus, for positive x_3 values, symmetry conditions

$$u_1(x_1, x_2, x_3) = u_1(-x_1, x_2, x_3), \quad (31a)$$

$$u_2(x_1, x_2, x_3) = -u_2(-x_1, x_2, x_3), \quad (31b)$$

$$u_3(x_1, x_2, x_3) = -u_3(-x_1, x_2, x_3), \quad (31c)$$

reduce the problem to a quarter space. Symmetry properties with respect to the plane $x_2 = 0$ with both x_1 and x_3 being positive

$$u_1(x_1, x_2, x_3) = u_1(x_1, -x_2, x_3), \quad (32a)$$

$$u_2(x_1, x_2, x_3) = -u_2(x_1, -x_2, x_3), \tag{32b}$$

$$u_3(x_1, x_2, x_3) = u_3(x_1, -x_2, x_3), \tag{32c}$$

reduce the analytical full space problem to one which can be simulated by examining one octant of the full space (one quarter of the circular fault) which we choose to be the octant for which $x_1, x_2,$ and x_3 are all positive quantities.

Figure 3 displays the analytical and numerical results for five values of $\tilde{x}_1 (\tilde{x}_1 = x_1/r_0)$. The analytical results (solid lines) which would linearly extend indefinitely have been terminated at the border of the figure. The numerical results (crosses) agree quite well with the analytical results at early times including the square root discontinuity which characterizes the arrival of the rupture front.

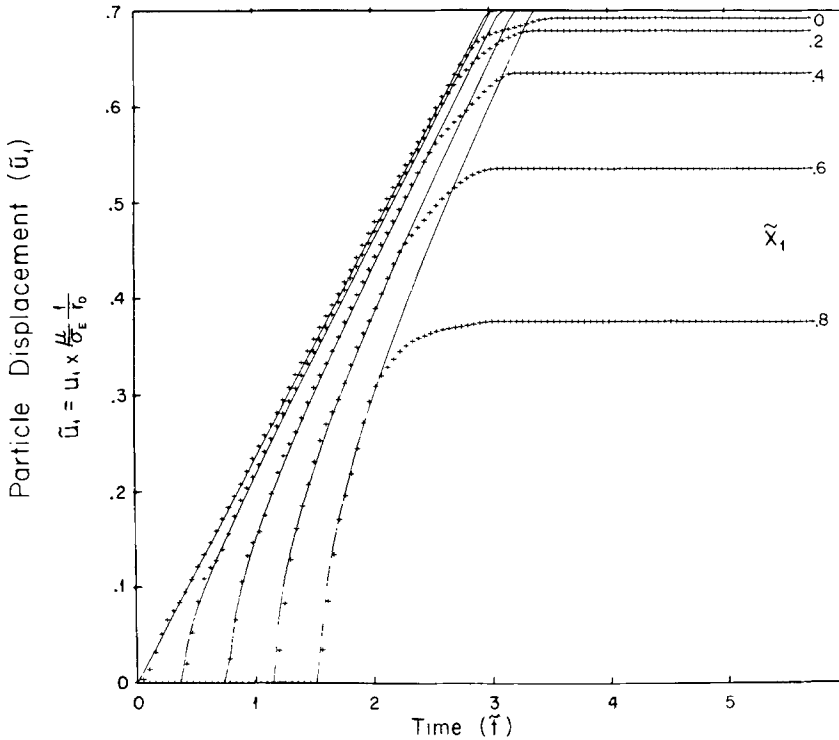


FIG. 3. Comparison at five locations of particle displacements obtained from Kostrov's (1964) self-similar rupture, $\nu = 0.9\beta$, with our finite element solution (crosses) for a circular fault of radius r_0 .

To quantify the agreement between the analytic solution and our finite element results we have computed the amplitude spectrum of displacement for our numerical results using a Fast Fourier Transform and derived the analytic Fourier transform of Kostrov's solution. The comparison in the frequency domain for points located at 0.1, 0.4, and 0.8 r_0 are shown in Figures 4, 5, and 6. The most important feature is that the numerical results accurately reproduce the high-frequency spectrum up to 2 Hz. This resolution in frequency is about four times greater than what one could expect from a finite element method propagating a wave. The frequency 2 Hz is approximately the inverse of the time taken for the rupture velocity to cross the diagonal of one element. The accuracy directly results from our method of relaxing the stress as the rupture front passes through an element, Appendix I. Basically the effective stress that contributes to the nodal force is weighted by the area that is encompassed by the rupture front. For example, a particle (node) within the

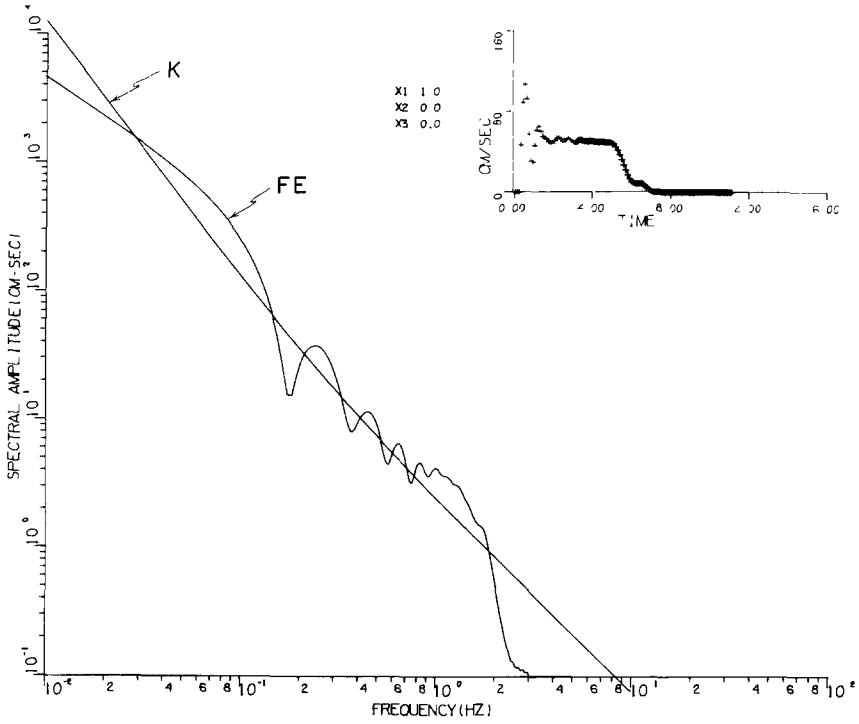


FIG. 4. For a particle at $0.1 r_0$ a comparison between the displacement amplitude spectrum from Kostrov's self-similar solution, labeled *K*, and from our finite element solution labeled *F.E.* for a circular fault. Numerical values used were $\beta = 3.0$ km/sec, $\nu = 0.9\beta$, $\alpha = \sqrt{3}\beta$, $\rho = 2.7$ gm/cm³, $r_0 = 10$ km, and $\sigma_E = 100$ bars. Inset shows time history of \dot{u}_1 at position (1, 0, 0).

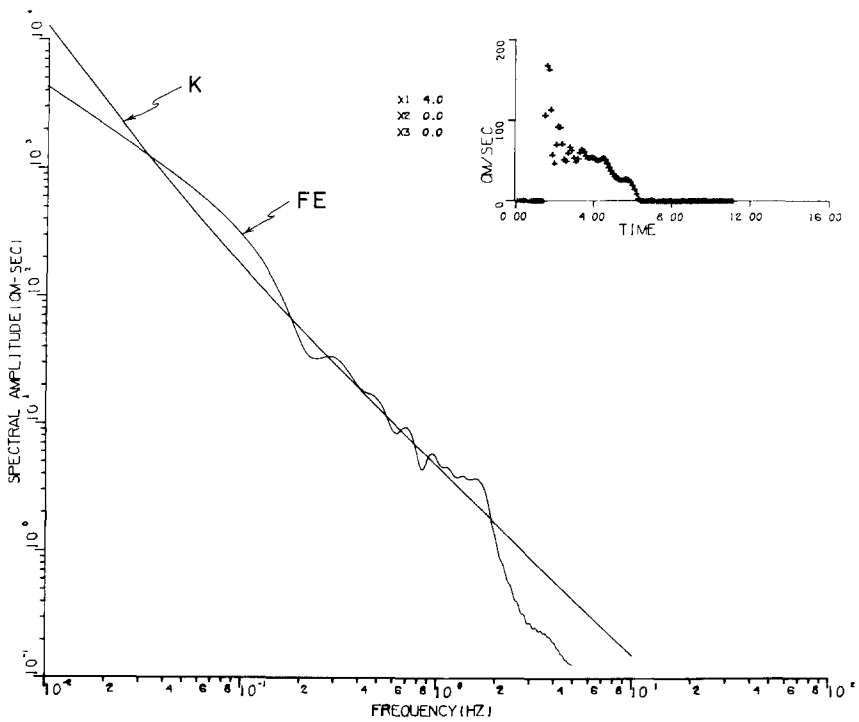


FIG. 5. See Figure 4 for caption. Particle at $0.4 r_0$.

prescribed fault boundary has four elemental areas that contribute to the effective stress. It is not until all of these areas are completely enclosed by the rupture front that the stress relaxation is complete. High resolution of the displacement function on the fault is important because this function can then be used as input for other methods which have a better capability of propagating waves, e.g., Green's functions, reflectivity, Fuchs and Müller (1971), or direct wave number integration, Apsel *et al.* (1977).

The analytic spectrum has a low frequency asymptote proportional to f^{-2} since the displacement grows linearly in time and a high frequency asymptote proportional to $f^{-3/2}$ as a result of the square root discontinuity at the initiation of the slip function. Because the numerical results are for a finite source, and the displacement has a nonzero static value, the numerical results have a low frequency asymptote of f^{-1} . The scale for the spectrum is determined using an effective stress of 100 bars.

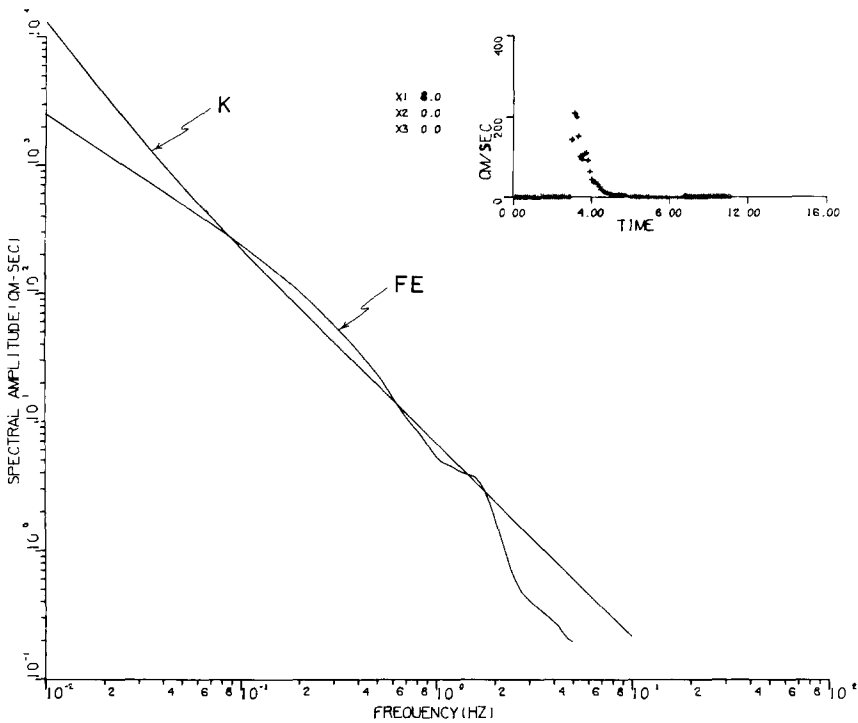


FIG. 6. See Figure 4 for caption. Particle at $0.8 r_0$.

An important consideration is the stopping phase. Near the initiation of rupture, e.g., $r = 0.1 r_0$, the dominant feature is the arrival of the rupture front; however, if the rupture stops abruptly at the boundary of the fault, the stopping phase can have a pronounced effect on the high-frequency end of the spectrum for points near the boundary. The numerical results deviate from the analytical solution at times $t > \tau$ where

$$\tau = r_0/v + \frac{r_0 - \sqrt{x_1^2 + x_2^2}}{\alpha} \tag{33}$$

Thus the deviation at late time is caused by the finiteness of the fault; information

pertaining to the size of the fault initially propagates from the edge of the fault to an observer with the P -wave speed.

The distribution of static offsets is fit quite well by a curve

$$u_1 = (1.27) \left[\frac{12}{7\pi} \frac{\sigma_E}{\mu} \sqrt{r_0^2 - x_1^2} \right] \quad (34)$$

where the term in brackets is the static solution for a circular crack of radius r_0 , (Neuber, 1937; Keilis-Borok, 1959; Eshelby, 1957). Thus, if one were to infer a stress drop from measuring static displacements, the inferred stress drop would be 27 per cent too large. This overshoot in the static displacement has been noted before by Savage and Wood (1971) and was calculated by Madariaga (1976) though he found a 20 per cent overshoot.

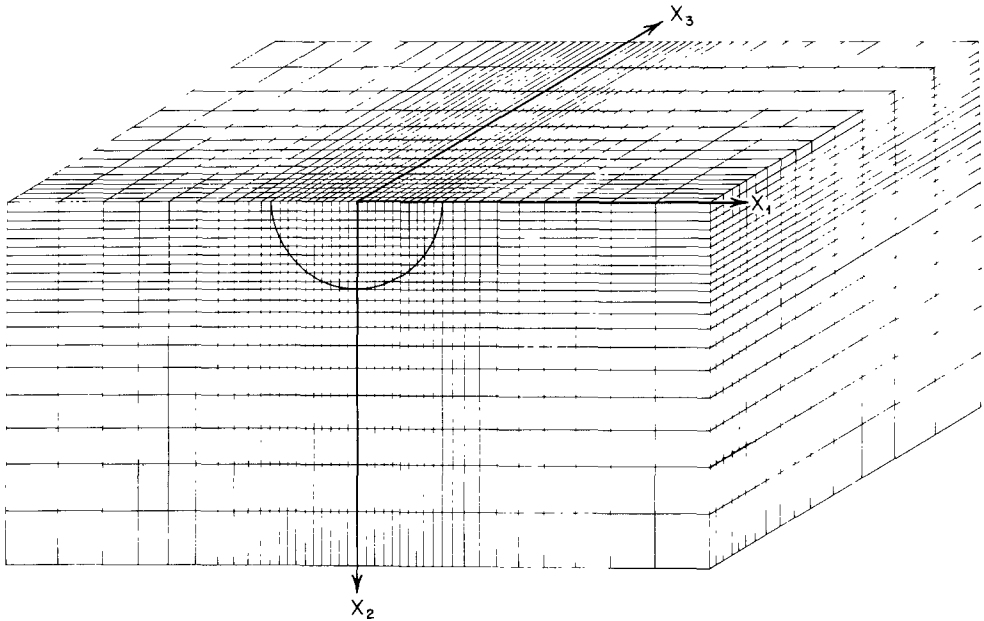


FIG. 7. Finite element grid used in this paper for simulating earthquakes. Because of symmetry conditions only one-half of the grid shown was used in computations.

HALF-SPACE COMPUTATIONS

Having satisfied ourselves that our finite element technique correctly executes our rupture model, we shall examine the near-field motion caused by a propagating stress drop over a vertical, semicircular fault which intersects the free surface. The first two ruptures which we shall discuss use the geometry and grid shown in Figure 7 which is the same grid used to simulate Kostrov's analytic solution.

For the rupture which nucleates at depth, we expanded the grid in the \hat{x}_2 direction by adding three additional rows of elements such that there are 12 rows of uniform elements and 11 rows of expanding elements. This was necessary to prevent P -wave reflections from returning from the boundary plane for which x_2 takes on its maximum values. Being substantially different, the geometry of the third rupture will be discussed later. Each rupture is bilateral allowing us to use only one-half of the grid shown in Figure 7. The grid used in the computations is 20 by 20 by 15 three-dimensional rectangular elements. The near-field volume 10 by 10 by 5 is

composed of cubical elements. Beyond this volume each element increases with a 20 per cent growth rate to place the outer boundaries at such a distance that a P wave cannot reflect from the outer boundary and return to contaminate the near-field motion.

SUBSONIC RUPTURE, SURFACE ORIGIN

First we consider a rupture which nucleates at the free surface and propagates subsonically until the whole fault plane has had a uniformly applied effective stress. Because the ground motion scales directly with the effective stress, we can set σ_E to any value, e.g., $\sigma_E = 1$ bar. However, the particle motion may or may not scale directly with rupture velocity. Hence, the results given in this section are applicable only for the specified rupture velocity, $v = 0.9\beta$.

To illustrate the particle motion (in our numerical scheme we store the time history of displacement for every point on the free surface and for every point on the fault surface) we have plotted in Figure 8 the individual time histories of particle displacement and particle velocity along the strike of the fault at the free surface.

First consider the particle displacements in Figure 8. Except for the node at the origin of the rupture (0, 0, 0) for which the displacement is linear in time, all of the displacements \tilde{u}_1 have a discontinuity in displacement which characterizes the arrival of the rupture front as in the self-similar rupture. We see that in magnitude the component \tilde{u}_1 dominates the vertical displacements (\tilde{u}_2) and the transverse displacements (\tilde{u}_3), the latter two being comparable in magnitude. In Figure 9 we have made a composite plot of \tilde{u}_1 versus \tilde{t} for ten points along the fault trace. These points are labeled 0 to 0.9 to indicate the ratio of their distance (r) from the origin to the radius (r_0) of the fault, e.g., 0.8 implies $r = 0.8 r_0$. Recall that in our rupture model a particle exactly on the fault boundary is constrained to have $\tilde{u}_1 = \tilde{u}_2 = 0$. The distribution of static offsets for \tilde{u}_1 is fit well by the static solution, see equation (34), provided the effective stress σ_E is multiplied by 1.25 to account for the dynamic overshoot (Savage and Wood, 1971).

The focusing of energy in the direction of propagation is clearly revealed in the particle velocity field. Witness the particle velocity \tilde{u}_1 tripling in magnitude from the origin to the outer boundary, Figure 10.

The particle velocity \tilde{u}_1 closely resembles the analytic form of the self-similar model. For example, the particle at (0, 0, 0) in Figure 10 shows a jump to a constant velocity indicative of the linear displacement time history. Looking at the particle $r_0 = 0.6$ in Figure 10 the square root discontinuity manifests itself as the jump which is followed by a decay with a square root dependence in time to a constant velocity. If the finite element solution had infinite frequency resolution, the particle velocity peak would theoretically be infinite.

The \tilde{x}_3 component of velocity reveals two interesting phenomena in Figure 8: (1) The long-period peak prominent at positions (0, 0, 0) through (5, 0, 0) appears to originate at the outer boundary of the fault and propagate toward the center (0, 0, 0); whereas the long-period trough late in the signal appears to move outward from the center. Since we have no numerical reflections from the outer boundaries of our finite element grid capable of arriving during that time period, we surmise that these phases are related to the healing of the fault. (2) The \tilde{x}_3 component displays the near-field horizontally polarized motion that travels at the P -wave speed. This near-field term in the particle velocity \tilde{u}_3 is seen clearly as the small depression preceding the large positive peak for particles at (9, 0, 0) (10, 0, 0), and (11, 0, 0) at which distance phases traveling at the P -wave speed and S -wave speed are well separated.

The exact time at which a point in the fault plane locks is not simply related to its distance from the fault boundary as it was in the full-space calculation. Also the free surface destroys any symmetry with respect to a 45° line through the origin in the fault plane. For example, nodes along the fault trace \hat{x}_1 axis have longer rise times than do points along the \hat{x}_2 axis. A major difference between our half-space computation and full-space solutions (Richards, 1973, 1976; Madariaga, 1976) is the

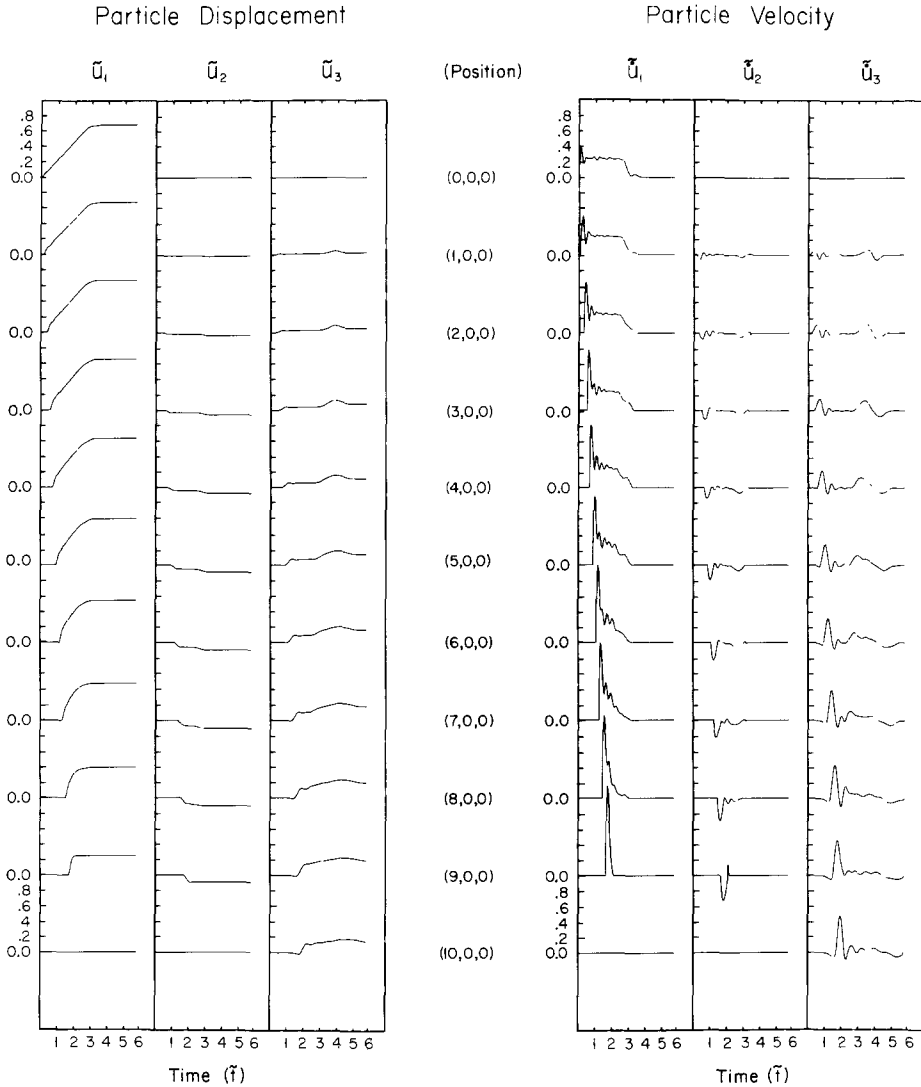


FIG. 8. The computed dimensionless particle displacements and velocities for 11 positions along the fault trace based on a subsonic rupture with a surface origin.

existence of u_2 and \dot{u}_2 even though we relieved only the S_{31} component of stress. The existence and magnitude of u_2 and \dot{u}_2 are precluded in full-space solutions and are elements which would violate Madariaga's (1976) scheme for reducing a three-dimensional problem to a two-dimensional computation.

Microzonation assessments are based on knowing the probable distribution of maximum, near-field, ground motion. Any number of variables, e.g., maximum

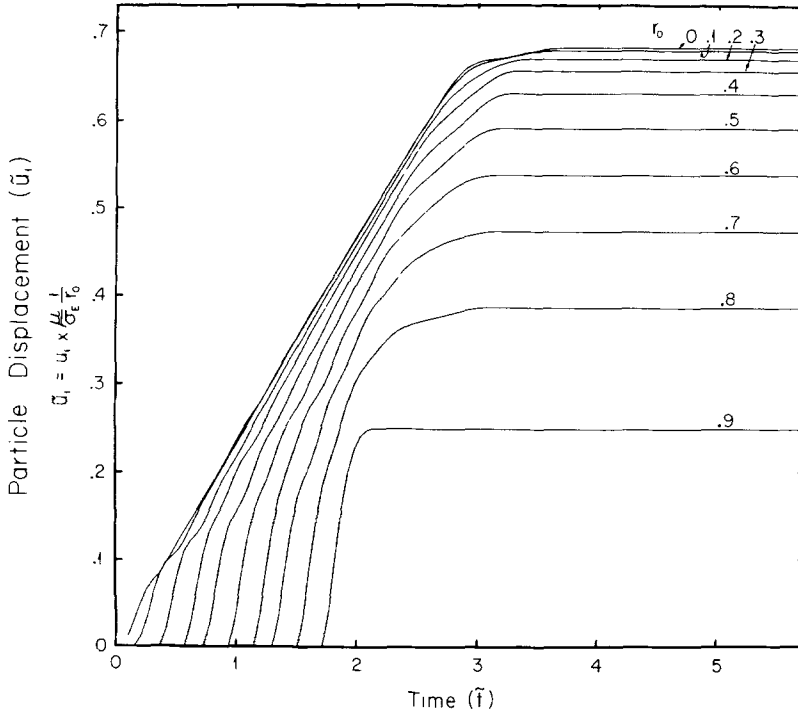


FIG. 9. A composite plot of time histories of dimensionless particle displacement \tilde{u}_i for positions along the fault trace. Displacements initiate with a square root discontinuity. Static values follow the elliptical shape predicted by static theory but show a 25 per cent overshoot above the theoretical values.

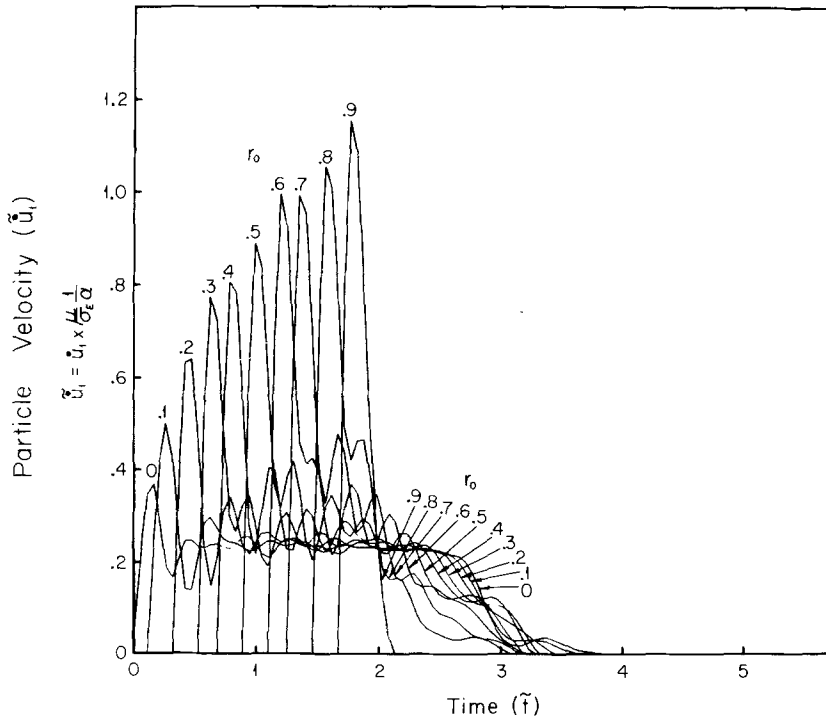


FIG. 10. A composite plot of time histories of dimensionless particle velocity \dot{u}_i for positions along the fault trace. Note the increase in amplitude in the direction of rupture propagation.

vertical displacement, or maximum particle velocity in the \hat{x}_1 direction, might be plotted as a function of position on the free surface. For this rupture we have plotted contours of the maximum horizontal particle velocity

$$\tilde{u}_H = \max\left[\sqrt{\tilde{u}_1^2(x, t) + \tilde{u}_3^2(x, t)}\right] \tag{35}$$

where $\max\left[\sqrt{\tilde{u}_1^2(x, t) + \tilde{u}_3^2(x, t)}\right]$ represents the maximum value of horizontal particle velocity attained at position $\mathbf{x} = (x_1, 0, x_3)$ and at any time t during the rupture process (Figure 11). Again we observe the focusing effect of rupture propagation as the double lobed pattern (bilateral rupture) is peaked at the ends of the

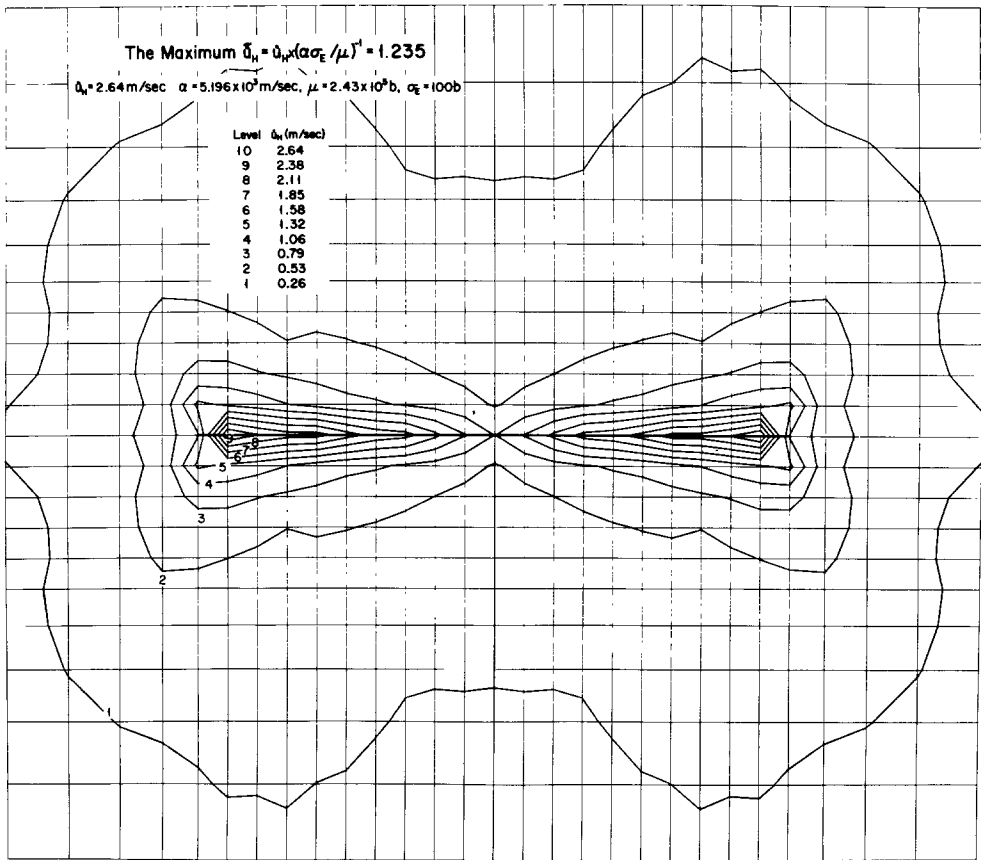


FIG. 11. Free surface contours of dimensionless peak horizontal particle velocity \tilde{u}_H resulting from a subsonic, strike-slip rupture which initiated at the free surface.

fault. We have labeled the contours with levels 1 through 9 which represent the percentage values 10 through 90 of the maximum value attained by any particle on the free surface. In dimensionless form, the maximum horizontal particle velocity on the surface is 1.235 which converts to 2.64 m/sec using our standard set of parameters: $\sigma_E = 100$ bars, $r_0 = 10$ km, $\alpha = 5.196$ km/sec, $u = 2.43 \times 10^9$ bars, and $\beta = \alpha/\sqrt{3}$. The entire free surface is not shown but everywhere else \tilde{u}_H is less than level 1.

SUBSONIC RUPTURE NUCLEATING AT DEPTH

A rupture which nucleates at depth embodies the full three-dimensional character of the particle motion. Particles on the free surface experience radiation prior to the rupture reaching the free surface. The effective rupture velocity along the free surface (the rupture phase velocity) can exceed the P -wave speed. We might also expect a breakout phase as the rupture front pierces the free surface, and we might expect to see a reflection from the free surface reinforce the particle motion on the fault plane at depth (Burrige and Halliday, 1971).

To assess the magnitude of these effects and to compare results with the subsonic rupture which nucleated at the surface, we initiated a rupture at the lowest point $(0, 10, 0)$ of the semicircular fault. We assigned a subsonic rupture velocity $v = 0.9\beta$. Since the rupture nucleates at depth, we expect the apparent rupture velocity for nodes along the surface to exceed our assigned value of 0.9β . Using the time elapsed between the rupture front first breaking the free surface at $(0, 0, 0)$ and the time when it reaches the edge of the fault $(10, 0, 0)$ we calculated an average apparent rupture velocity of 1.44α . The effect of this supersonic velocity is to create a nearly constant peak particle velocity for \tilde{u}_1 along the fault trace. We have also computed the particle motion for a rupture with the same fault geometry but with $v = \infty$ (Archuleta, 1976); for the instantaneous rupture the particle velocity was nearly constant along the fault trace. The nearly constant amplitude of \tilde{u}_1 in Figure 12 can be contrasted with the surface rupture which showed a monotonic increase for \tilde{u}_1 along the fault trace. The ratio of the magnitude of \tilde{u}_1 for the rupture beginning at depth compared to the rupture initiating at the surface ranges between 500 and 40 per cent, depending on which point along the fault is taken. Since the instantaneous rupture (Archuleta, 1976) did not produce particle velocities exceeding the maximum \tilde{u}_1 caused by the surface focus rupture, we could not attribute the values of \tilde{u}_1 to the supersonic rupture phase velocity. The cause of these large particle velocities is a combination of the piercing of the free surface by the rupture front, the breakout phase, and focusing of energy in the direction of propagation as revealed in Figure 13, in which particle velocities for points $(0, 0, 0)$ to $(0, 9, 0)$ i.e., particles along the \hat{x}_2 axis, are plotted. Compare the general increase in particle velocity magnitude as the rupture progresses toward the free surface with Figure 10 for the subsonic rupture which initiated at the surface. Until the rupture pierces the free surface, the magnitude of the particle velocity parallels the increase we have attributed to focusing in the surface focus rupture. The free surface is prominently identified by the almost doubling in size of the particle velocity.

Even though \tilde{u}_1 is relatively constant along the fault trace, \tilde{u}_2 and \tilde{u}_3 (Figure 12) show a linear trend. Eshelby's (1957) static solution for the displacement component \tilde{u}_3 is linearly related to the distance along the fault trace, but it is uncertain why \tilde{u}_3 or \tilde{u}_2 show such a linear trend. This linear trend is also evident in the surface focus rupture although the slope is less.

A second effect of the free surface is to generate a reflected phase which manifests itself as the long-period bump late in time in Figure 13. In the two-dimensional model of Burrige and Halliday (1971) the reflected phase accelerated the particle motion. This extra impetus is clearly evident in Figure 14 where we see late in time the particle displacement for points $(0, 0, 0)$ to $(0, 9, 0)$ surge briefly before attaining its static value. The reflected phase clearly prolongs the particle motion on the fault surface at depth. However, the static value of displacement \tilde{u}_1 for points along the fault trace is well fit by the static solution of Neuber (1937)/Eshelby (1957) provided

that the effective stress σ_E is multiplied by 1.2 to obtain the static stress drop $\Delta\sigma$. The multiplicative factor 1.2 is not so different from the 1.25 of the surface origin rupture. Although a rupture nucleating at depth has a pronounced effect on the particle velocity field, it has almost no effect on the static displacement field.

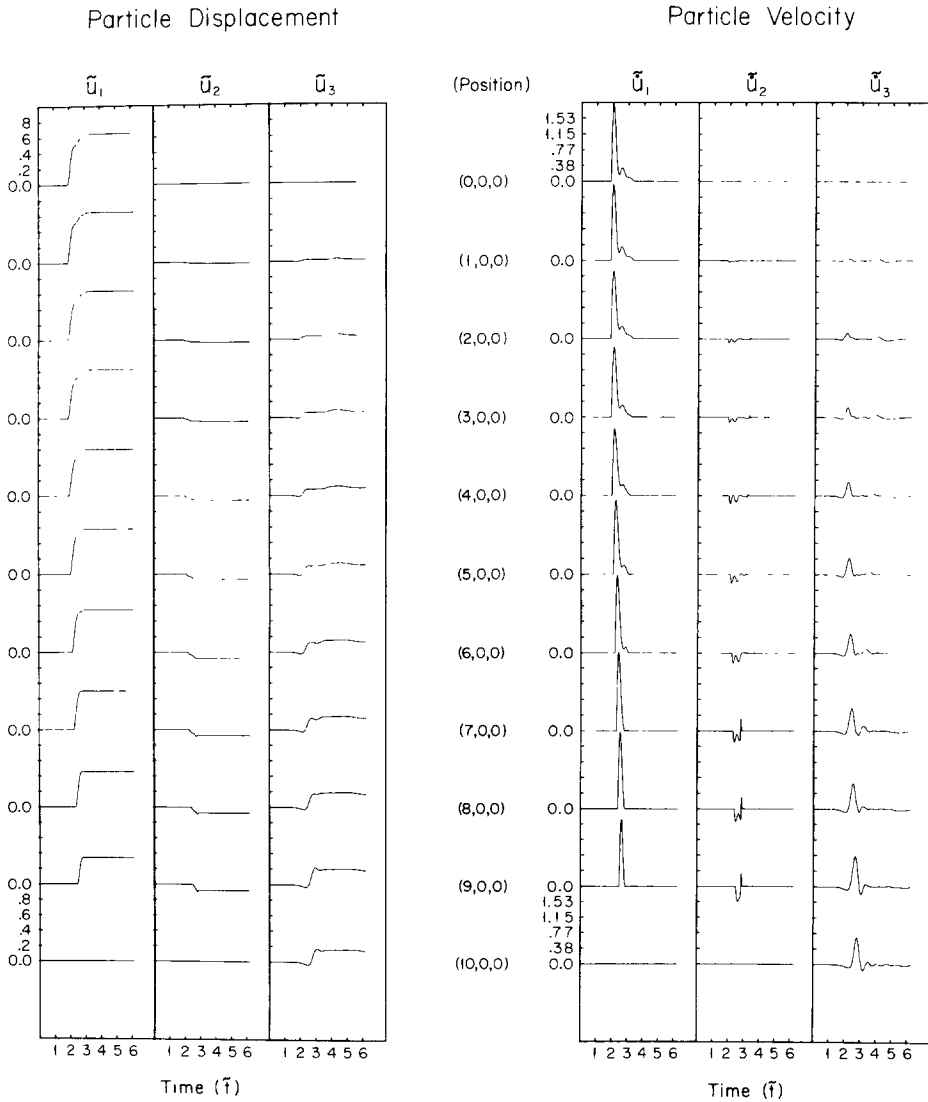


FIG. 12. Computed dimensionless particle displacements and velocities for 11 positions on the fault trace based on a subsonic, strike-slip rupture which nucleated at depth.

For the purpose of studying the effects of radiation prior to the rupture front breaking the free surface, we have plotted Figure 15, the particle displacements and particle velocities at 11 locations $(0, 0, 5)$ through $(10, 0, 5)$, points which run parallel to the fault trace. The scales in Figure 15 are one-half of the scale for particle displacement and one-fifth of the scale for particle velocity in Figure 12, respectively. Figure 15 reveals an assortment of interesting phenomena. One of the more interesting is the presence of the near-field shear motion traveling at the P -wave speed. This near-field characteristic shows itself as the small negative phase preceding the

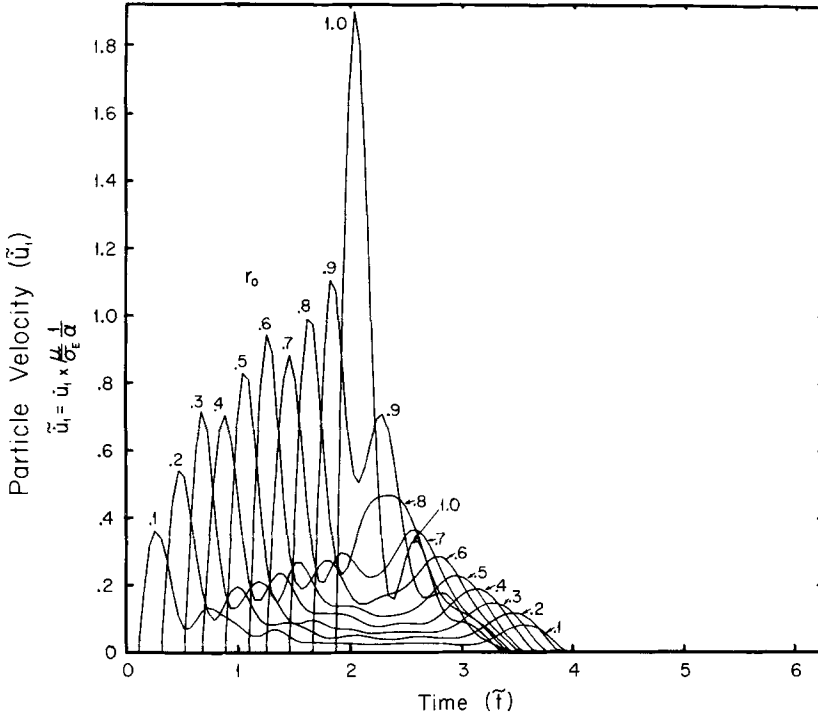


FIG. 13. Composite plot of time histories of particle velocity \tilde{u}_1 for points at depth on the x_2 axis measured from the rupture origin $(0, 10, 0)$. The rupture focuses energy in the direction of propagation. The free surface causes the particle velocity to almost double in amplitude.

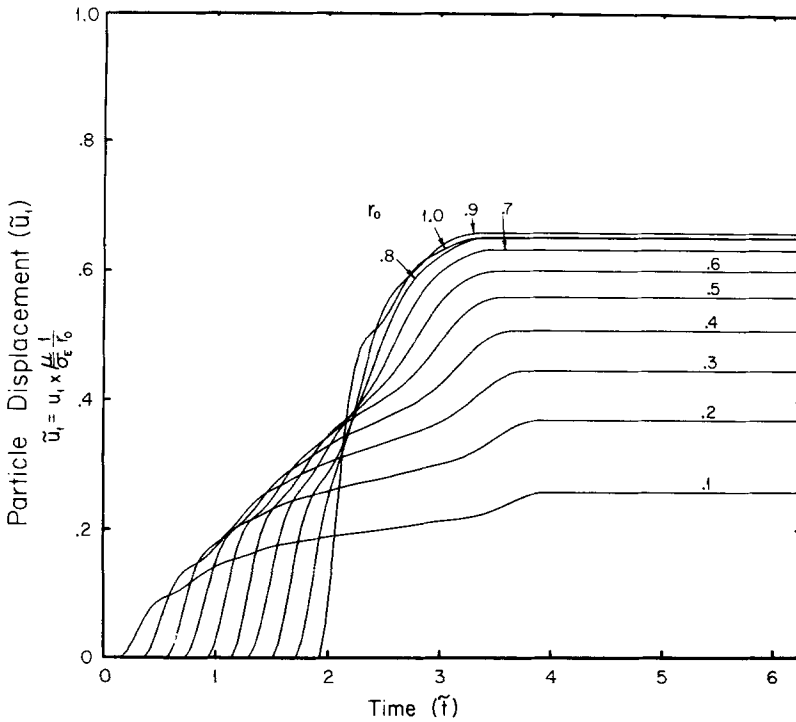


FIG. 14. Composite plot of time histories of particle displacement u_1 for points at depth on the x_2 axis measured from the rupture origin $(0, 10, 0)$. The late time bump is caused by the surface reflection.

large positive motion clearly seen at position (0, 0, 5). The same near-field phase is evident in \tilde{u}_3 at position (10, 0, 0) in Figure 8. This phase has the same radiation pattern as a horizontally polarized *S*-wave but of opposite sign, i.e., a $\cos 2\phi$ distribution where ϕ is the azimuthal angle measured from the normal to the fault. The dying out of this phase as we examine positions (0, 0, 5) through (5, 0, 5) is consistent with a $\cos 2\phi$ radiation pattern.

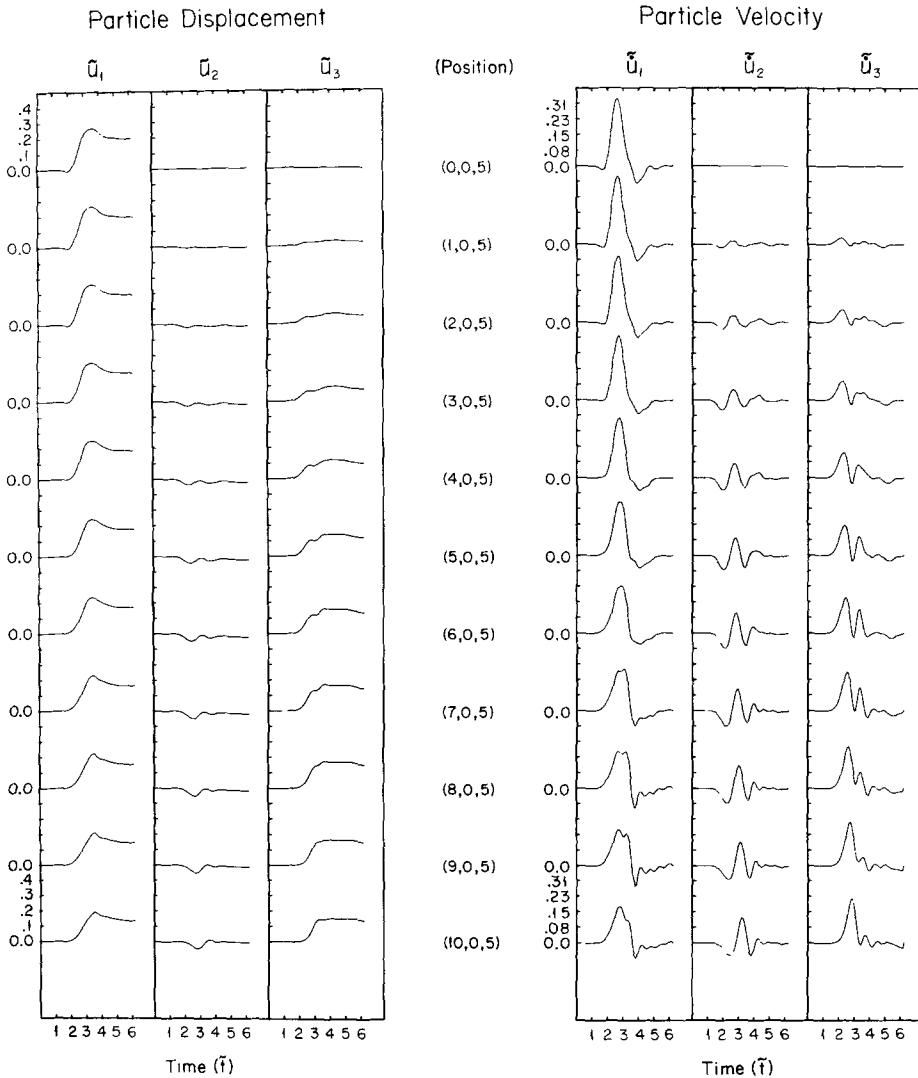


FIG. 15. Computed dimensionless particle displacements and velocities for 11 positions 5 elements off the fault trace. Values are based on subsonic rupture nucleating at depth.

The best indicator of phases associated with the rupture front breaking through the free surface is the surge in the particle displacement \tilde{u}_3 . The timing of this additional positive displacement coincides with an *S*-wave arriving from the nearest point on the fault. In \tilde{u}_3 this phase is clearly seen at positions (5, 0, 5) to (7, 0, 5) as the emergent, second, positive peak. The arrival of the *S* wave is also recorded in \tilde{u}_1 as a small dip at the peak observed at positions (8, 0, 5) through (10, 0, 5).

We observe the diffraction of waves by the fault as the static value of \tilde{u}_1 is less

than the maximum. The static value of \tilde{u}_3 is comparable to \tilde{u}_1 for positions (5, 0, 5) through (10, 0, 5) whereas the static value of \tilde{u}_2 is nearly zero. Looking at the corresponding particle velocities we note that \tilde{u}_1 and \tilde{u}_3 are comparable with \tilde{u}_2 , only slightly smaller. From these time functions of particle displacement and particle velocity we could assume that the \hat{x}_1 component of motion decays more rapidly with distance than do the \hat{x}_2 and \hat{x}_3 components of motion at least to a distance comparable to r_0 . One can also see from the magnitudes of particle displacement and particle velocity that the particle velocity decreases in magnitude more quickly with distance from the fault than does particle displacement; this is especially true for the \hat{x}_1 component of motion.

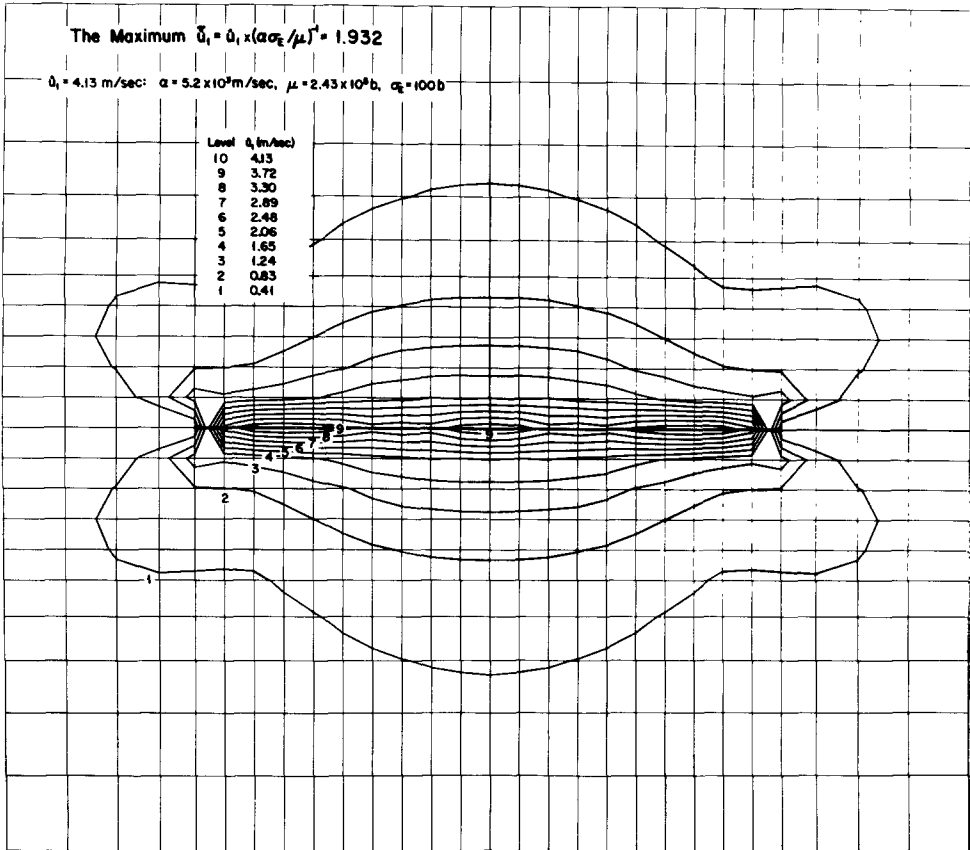


FIG. 16. Free surface contours of dimensionless peak particle velocity parallel to the fault strike $|\tilde{u}_1|$ for a subsonic rupture nucleating at depth.

To illustrate the behavior of the free surface we have displayed in Figures 16, 17, 18, 19, the contours of maximum velocity for $|\tilde{u}_1|$, $|\tilde{u}_2|$, $|\tilde{u}_3|$, and \tilde{u}_H [previously defined in equation (35)], respectively. In each figure the contours are labeled 1 through 9 representing the levels 10 per cent of absolute maximum through 90 per cent of absolute maximum. The absolute maximum is the largest absolute value of the variable being contoured. For example, the largest absolute value of \tilde{u}_1 anywhere on the free surface is 1.932 in dimensionless form, equal to 4.13 m/sec for our standard set of parameters for the medium and the fault. Because \tilde{u}_1 is dominant, due to the breakout phase of the free surface coupled with a supersonic rupture phase velocity, the contours of maximum horizontal velocity, Figure 19, are quite

uniform with no resemblance to the double-lobed pattern in Figure 11. The values of the contours in Figure 19 are considerably larger than in Figure 11; in fact, the 60 per cent contour in Figure 19 is equivalent to the maximum contour in Figure 11. The vertical and transverse components are similar in appearance, but the vertical component is required by symmetry to be zero for points beyond the ends of the fault and along its strike. The absolute maximum of \tilde{u}_2 is almost one-half the absolute maximum of \tilde{u}_3 . An important aspect of $|\tilde{u}_2|$ and $|\tilde{u}_3|$ is that both decay with distance less rapidly than $|\tilde{u}_1|$.

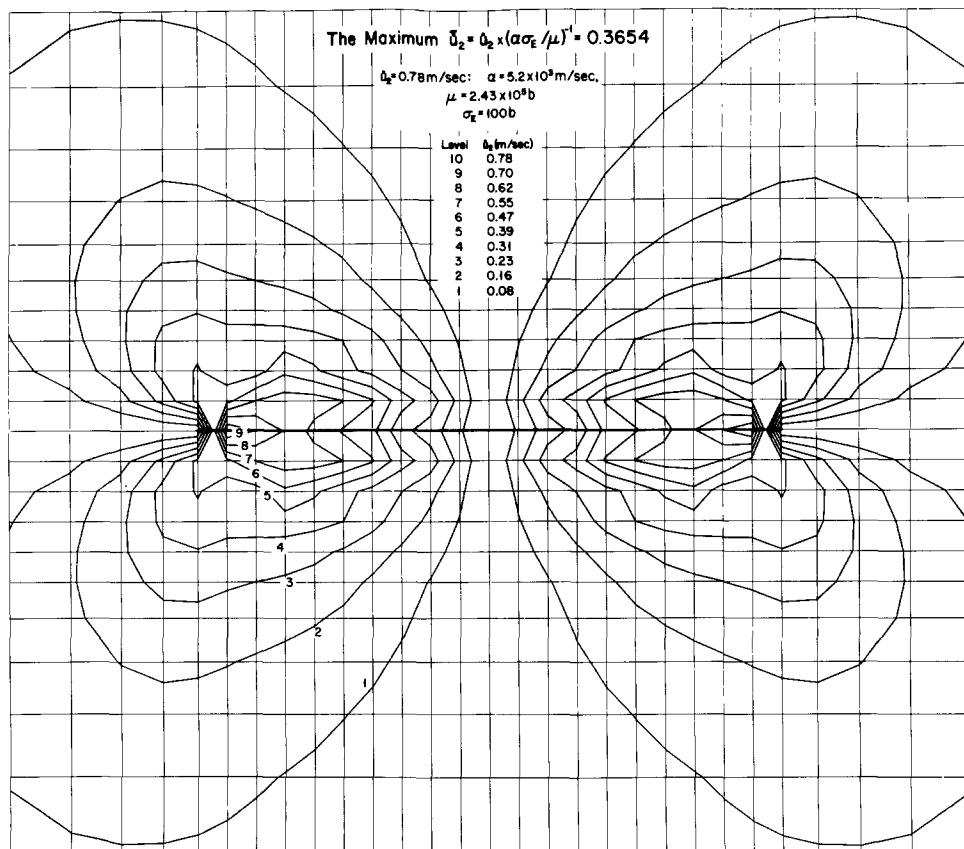


FIG. 17. Free surface contours of dimensionless peak particle velocity normal to the free surface $|\tilde{u}_2|$ for a subsonic rupture nucleating at depth.

RUPTURE ANALOGOUS TO FOAM RUBBER EXPERIMENT

As the final numerical simulation we sought to reproduce the particle displacement measurements caused by a stick-slip event on a semicircular fault in foam rubber (Archuleta and Brune, 1975). This simulation differs in one major aspect from our previous simulations: the rupture in the foam rubber experiment was primarily unilateral. A unilateral rupture destroys a symmetry condition. We are required to use grid everywhere on one side of the fault. Because this problem required such a large number of elements, we had to reduce the number of elements (for budgetary reasons) on a fault radius from ten to four. Thus, we have considerably less spacial information along the fault.

Based on the observations, we initiated the rupture at the free surface at a distance midway between one end of the fault and its center. We specified an

effective stress of 0.0015μ and a rupture velocity of 0.74β (0.74β appears to be a better fit to the data than 0.7β previously given by Archuleta and Brune, 1975). A comparison of the finite element particle displacements, continuous lines, and the measured particle displacements, discrete triangles, is shown in Figure 20. Foam rubber displacement time functions show a general tendency to start abruptly but then change to a more gentle slope. The measured static values agree quite well with the numerical results. The major discrepancy is the rise times of the numerical results especially near the initiation point and the first points to rupture. The numerical particle displacements attain their static values in approximately one-half the measured time. After the rupture has propagated a distance of about $\frac{3}{8} r_0$, the discrepancy in rise times diminishes. We can speculate as to the cause of the discrepancy in rise times. Since the measurements were for targets positioned

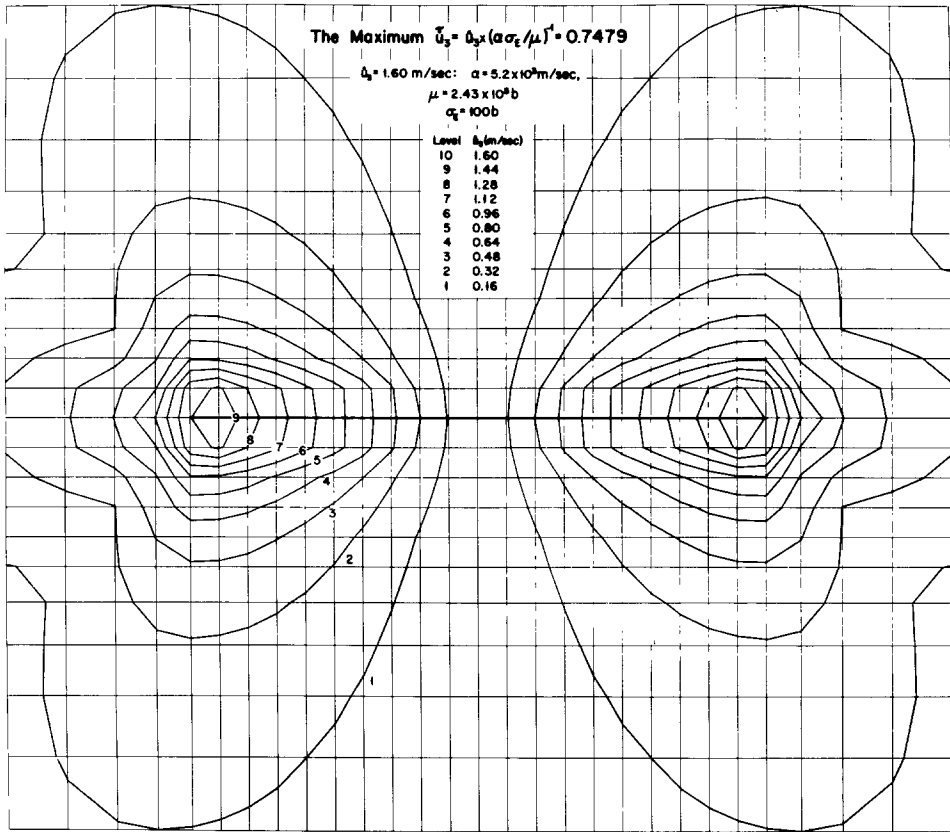


FIG. 18. Free surface contours of dimensionless peak particle velocity normal to the fault plane $|\tilde{u}_3|$ for a subsonic rupture nucleating at depth.

slightly off the fault (a distance approximately $\frac{1}{16} r_0$), particle velocities from the numerical simulation must be reduced whereas the static displacements could remain unaltered. For example, recall the difference in scales for particle displacement and velocity for points off the fault in the rupture which nucleated at depth. A second conjecture is that the fault was not in a state of uniform prestress. Although the entire fault was subject to an average stress change near 0.15μ , locally the stress available to accelerate the particles differed from area to area on the fault plane. A third alternative is that the frictional characteristics of foam rubber are

velocity or displacement dependent. In such a case a simple Coulomb-friction relationship, such as that used in the finite element method where the frictional shear stress is directly related to the normal stress, is not a sufficient representation of the frictional behavior. The agreement between the measured displacement time histories and those computed using our earthquake model leads us to consider additional physical processes which can influence the rupture. Still the agreement is not so bad that we think our model is entirely inapplicable to our experiments.

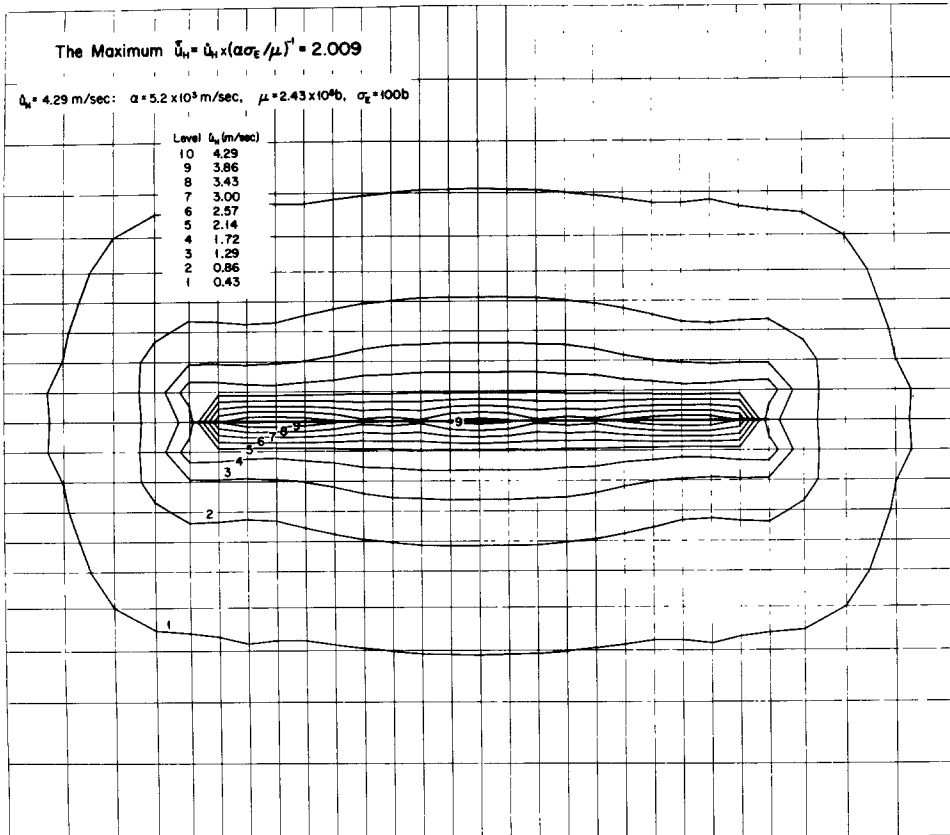


FIG. 19. Free surface contours of dimensionless peak horizontal particle velocity \dot{u}_H for a subsonic rupture nucleating at depth.

SUMMARY

We would like to review the principal results presented in this paper and to present research topics which can be approached using our basic numerical scheme. Perhaps the major result of this paper is the presentation of a method for simulating earthquakes based upon a dynamic, propagating stress drop over a finite plane in a three-dimensional, semi-infinite medium. We verified our method by comparing the numerical results with Kostrov's (1964) self-similar solution for a constantly expanding shear fracture in a full space.

To illustrate the method we simulated two strike-slip earthquakes for which the initial conditions differed only in the hypocentral location. Nevertheless, the ensuing near-field ground motion differed considerably both in amplitude and distribution. The rupture which nucleated at the free surface showed a pronounced focusing in

the direction of rupture propagation. Particle velocities attained values on the order of 2.5 m/sec for a fracture with a 100 bar effective stress propagating with a velocity of 2.7 km/sec over a fault 10 km in radius, embedded within a Poisson solid with shear-wave velocity of 3 km/sec.

The ground motion for the rupture which initiated at depth was dominated by the amplification caused by the rupture piercing the free surface. The free-surface distribution of particle velocity revealed a uniform distribution with maximum

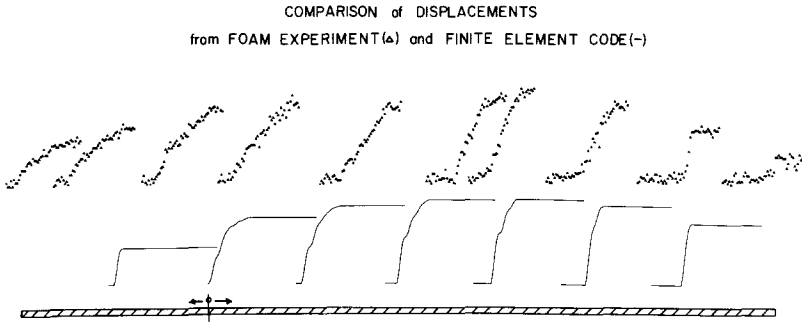


FIG. 20. A comparison of foam rubber displacement time histories (triangles) with computed particle displacements, u_1 for points along the fault trace.

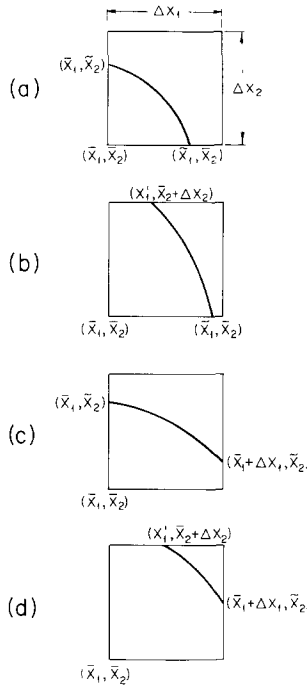


FIG. 21. A pictorial view of four possible intersections of the rupture front and the finite element boundaries.

values on the order of 4 m/sec. Examination of the particle velocity on the fault plane at depth showed that the rupture did focus energy in the direction of propagation similar in magnitude to the rupture which initiated at the free surface. The distribution and magnitude for the near-field particle velocities were attributed

to the amplification caused by the free surface and the apparent supersonic rupture velocity along the free surface. The distribution of static displacements did not vary significantly from those produced by the surface nucleation.

The method allows many possibilities for future work some of which we have already begun. We can examine effects such as nonuniform stress, spacially varying friction, normal and thrust faulting, corner frequency relationships, structural heterogeneities, and different failure mechanisms such as fracture energy or velocity-dependent friction. Naturally we shall attempt to synthesize strong motion records from earthquakes such as the 1966 Parkfield (Archuleta and Day, in preparation) and 1940 El Centro.

ACKNOWLEDGMENTS

The authors are indebted to Steven Day for his many valuable comments throughout the preparation of this paper. The authors also wish to thank Jim Brune for his counsel during the course of this research. This work was sponsored in part by the grant from Research Applied to National Needs, National Science Foundation Grant NSF AEN74-13264, and is a contribution of the Scripps Institution of Oceanography.

APPENDIX I

CALCULATING NODAL FORCES WHICH RESULT FROM AN EFFECTIVE STRESS

Basically we select a point within the specified $\partial\Sigma$ for the nucleation of the rupture. The fault plane Σ consists of faces of elements as seen in Figure 2. Having specified the hypocenter and a rupture velocity, we advance the rupture front a distance $\mathbf{r} = \mathbf{v}\Delta t$, where Δt is the time step so that after N time steps, $\mathbf{r} = \mathbf{v}N\Delta t$. As the rupture front encompasses more area of the fault plane, we relax the shear stress on the newly fractured area. The change in shear stress is composed of two parts. One part is the stress caused by prior radiation; the other part is the effective stress. The force arising from the prior radiation stress is accounted for naturally in the finite element method through the stiffness matrix in equation (25). The change in shear stress related to the effective stress is denoted by τ and must be converted from a traction to a nodal (particle) force \mathbf{F}_n . In general τ is given by

$$\tau(\mathbf{x}, t) = (\sigma_E \cos \theta, \sigma_E \sin \theta, 0) \quad (\text{A1})$$

where $\tan \theta = \dot{s}_2(\mathbf{x}, t)/\dot{s}_1(\mathbf{x}, t)$. The force due to $\tau(\mathbf{x}, t)$ that is applied to node n is

$$\mathbf{F}_n = \sum_{e=1}^g \int_{S_e^{(n)}} \tau(t) a_n^e(\mathbf{x}) ds, \quad (\text{A2})$$

where $a_n^e(\mathbf{x})$ is the appropriate interpolation for node n throughout adjacent element e . The i th component of displacement $u_i(\mathbf{x}, t)$ within an element e is given as the summation of the nodal values $U_{in}(t)$ weighted by some interpolation function $a_n^e(\mathbf{x})$

$$u_i(\mathbf{x}, t) = a_n^e(\mathbf{x}) U_{in}(t). \quad (\text{A3})$$

The sum in equation (A2) extends over those elemental areas which are contiguous with the node n . The integration includes only that part of the elemental area which

is within both the rupture front and within the geometrical fault boundary shown as the cross-hatched area in Figure 2. For a node which has elemental areas that are completely within the geometrical fault boundary and within the rupture front, the effective nodal force is

$$\mathbf{F}_n = \sigma_E \cdot A^e(1, 0, 0) \tag{A4}$$

where A^e is the area of one element. The details for calculating the effective force using an arbitrary area S_e^e weighted by the interpolation functions are given below.

We wish to evaluate equation (A2). We are assuming that the finite element is a rectangular brick, and that everywhere within the fault area each element is identical in size and shape to every other element in the fault area. These restrictions could be relaxed, but they simplify the algebra. At first we shall limit our discussion to the geometry shown in Figure 2 in which four elemental areas contribute to the effective nodal force, $\mathcal{E} = 4$. In our finite element method we use a bilinear interpolation function

$$a_n^e(\mathbf{x}) = b_1 + b_2x_1 + b_3x_2 + b_4x_1x_2. \tag{A5}$$

We let the position of the node n at which we wish to calculate \mathbf{F}_n be $(\bar{x}_1, \bar{x}_2, 0)$ at some time t . The four interpolation functions are

$$a_n^1 = 1 - (x_1 - \bar{x}_1)/\Delta x_1 - (x_2 - \bar{x}_2)/\Delta x_2 + \frac{(x_1 - \bar{x}_1)(x_2 - \bar{x}_2)}{\Delta x_1 \Delta x_2} \tag{A6}$$

$$a_n^2 = 1 - (\bar{x}_1 - x_1)/\Delta x_1 - (x_2 - \bar{x}_2)/\Delta x_2 + \frac{(\bar{x}_1 - x_1)(x_2 - \bar{x}_2)}{\Delta x_1 \Delta x_2} \tag{A7}$$

$$a_n^3 = 1 - (\bar{x}_1 - x_1)/\Delta x_1 - (\bar{x}_2 - x_2)/\Delta x_2 + \frac{(\bar{x}_1 - x_1)(\bar{x}_2 - x_2)}{\Delta x_1 \Delta x_2} \tag{A8}$$

$$a_n^4 = 1 - (x_1 - \bar{x}_1)/\Delta x_1 - (\bar{x}_2 - x_2)/\Delta x_2 + \frac{(x_1 - \bar{x}_1)(\bar{x}_2 - x_2)}{\Delta x_1 \Delta x_2} \tag{A9}$$

subject to the conditions

$$a_n^e(\mathbf{x}) = 0, \quad e = 1, 4 \tag{A10}$$

whenever

$$x_1 \geq \bar{x}_1 + \Delta x_1 \tag{A11}$$

or

$$x_2 \geq \bar{x}_2 + \Delta x_2 \tag{A12}$$

where Δx_1 and Δx_2 are the widths of the element in the \hat{x}_1 and \hat{x}_2 directions, respectively.

The elemental areas which contribute to the integral are determined by the rupture front which is the locus of points (x_1, x_2) satisfying

$$(x_1 - x_1')^2/v_1^2 t^2 + (x_2 - x_2')^2/v_2^2 t^2 = 1 \quad (\text{A13})$$

where (x_1', x_2') is the origin for the rupture and v_1 and v_2 are the components of the rupture velocity in the $\hat{\mathbf{x}}_1$ and $\hat{\mathbf{x}}_2$ directions, respectively. To facilitate the algebraic manipulations, we transform to a new coordinate system whose origin coincides with the rupture origin

$$x_1 = x_1 - x_1', \quad (\text{A14a})$$

$$x_2 = x_2 - x_2'. \quad (\text{A14b})$$

(We will not introduce a new variable for the transformed system. The interpolation functions remain unchanged.)

We assume that τ does not depend on position within an element; thus, we can factor τ outside of the integral. With this application we write the expression for the effective force as

$$\mathbf{F}_n = \sum_{e=1}^4 \tau \iint dx_1 dx_2 a^e(x_1, x_2). \quad (\text{A15})$$

Each double integral in the sum involves four simple integrals of the type

$$I_1 = \iint dx_1 dx_2, \quad (\text{A16})$$

$$I_2 = \iint dx_1 dx_2 x_1, \quad (\text{A17})$$

$$I_3 = \iint dx_1 dx_2 x_2, \quad (\text{A18})$$

$$I_4 = \iint dx_1 dx_2 x_1 x_2. \quad (\text{A19})$$

The limits of integration depend on the intersection of the rupture front with the boundaries of the element. The four types of intersections are pictured in Figure 21. The most general type of intersection is shown in (b) which we will use as an example in evaluating the integrals I_1 , I_2 , I_3 , and I_4 . Depending on the proper interpolation function, the contribution (b) makes toward the effective force is

$$I = \tau \int_{\tilde{x}_1}^{x_1'} \int_{\tilde{x}_2}^{\tilde{x}_2 + \Delta x_2} dx_1 dx_2 a^i(\mathbf{x}) + \tau \int_{x_1'}^{\tilde{x}_1} \int_{\tilde{x}_2}^{\tilde{x}_2} dx_1 dx_2 a^i(\mathbf{x}), \quad (\text{A20})$$

where

$$x_1' = v_1/v_2 \sqrt{v_2^2 t^2 - (\tilde{x}_2 + \Delta x_2)^2}, \quad (\text{A21})$$

$$\tilde{x}_1 = v_1/v_2 \sqrt{v_2^2 t^2 - \tilde{x}_2^2} \quad (\text{A22})$$

and

$$\tilde{x}_2 = v_2/v_1 \sqrt{v_1^2 t^2 - x_1'^2}. \quad (\text{A23})$$

Using the above limits of integration the integrals I_1 , I_2 , I_3 , and I_4 become

$$I_1 = (x_1' - \bar{x}_1)\Delta x_2 - (\bar{x}_1 - x_1')\bar{x}_2 + v_2/2v_1 \{ \bar{x}_1 \sqrt{v_1^2 t^2 - \bar{x}_1^2} - x_1' \sqrt{v_1^2 t^2 - x_1'^2} + v_1^2 t^2 (\sin^{-1} \bar{x}_1/v_1 t - \sin^{-1} x_1'/v_1 t) \}, \quad (A24)$$

$$I_2 = \frac{1}{2} \{ (x_1'^2 - x_2'^2)\Delta x_2 - (\bar{x}_1^2 - x_1'^2)\bar{x}_2 \} - v_2/3v_1 \{ (v_1^2 t^2 - \bar{x}_1^2)^{3/2} - (v_1^2 t^2 - x_1'^2)^{3/2} \}, \quad (A25)$$

$$I_3 = \frac{1}{2} \{ (x_1' - \bar{x}_1)(2\bar{x}_2\Delta x_2 + (\Delta x_2)^2) - (\bar{x}_1 - x_1')\bar{x}_2^2 \} + v_2^2/2v_1^2 \{ v_1^2 t^2 (\bar{x}_1 - x_1') - \frac{1}{3}(\bar{x}_1^3 - x_1'^3) \}, \quad (A26)$$

$$I_4 = \frac{1}{4} \{ (x_1'^2 - \bar{x}_1^2)(2\bar{x}_2\Delta x_2 + (\Delta x_2)^2) - (\bar{x}_1^2 - x_1'^2)\bar{x}_2^2 \} + v_2^2/8v_1^2 \{ 2v_1^2 t^2 (\bar{x}_1^2 - x_1'^2) - (\bar{x}_1^4 - x_1'^4) \}. \quad (A27)$$

Using the appropriate coefficients (b_1, b_2, b_3, b_4) which depend on the particular interpolation function, the integral in (A20) becomes

$$I = \tau(b_1 I_1 + b_2 I_2 + b_3 I_3 + b_4 I_4). \quad (A28)$$

After this calculation is repeated for each elemental area which is contiguous to the node at $(\bar{x}_1, \bar{x}_2, 0)$, the results of the calculations are added to give the effective nodal force which is equivalent to an effective stress applied to the elemental areas. These calculations are performed at each time step for every node within the rupture front.

REFERENCES

- Aki, K. (1968). Seismic displacements near a fault, *J. Geophys. Res.* **73**, 5359-5376.
- Anderson, J. G. and P. G. Richards (1975). Comparison of strong ground motion from several dislocation models, *Geophys. J.* **42**, 347-373.
- Andrews, D. J. (1976). Rupture velocity of plane-strain shear cracks, *J. Geophys. Res.* **81**, 5679-5687.
- Apsel, R. J., J. E. Luco, and J. A. Orcutt (1977). Body wave and surface wave propagation in a multilayered half-space (abstract), Cordillerian Sect., *Geol. Soc. Am.* **9**, 381.
- Archuleta, R. J. (1976). Experimental and numerical three-dimensional simulations of strike-slip earthquakes, *Ph.D. Dissertation*, University of California, San Diego.
- Archuleta, R. J. and J. N. Brune (1975). Surface strong motion associated with a stick-slip event in a foam rubber model of earthquakes, *Bull. Seism. Soc. Am.* **65**, 1059-1071.
- Bache, T. C., J. T. Cherry, D. G. Lambert, J. F. Masso, and J. M. Savino (1976). A deterministic methodology for discriminating between earthquakes and underground nuclear explosions, *Systems, Science and Software Report SSS-R-76-2925*.
- Boore, D. M., K. Aki, and T. Todd (1971). A two-dimensional moving dislocation model for a strike-slip fault, *Bull. Seism. Soc. Am.* **61**, 177-194.
- Burridge, R. (1969). The numerical solution of certain integral equations with non-integrable kernels arising in the theory of crack propagation and elastic wave diffraction, *Phil. Trans. Roy. Soc. (London), Ser. A*, **265**, 353-381.
- Burridge, R. and J. Willis (1969). The self-similar problem of the expanding elliptical crack in an anisotropic solid, *Proc. Cambridge Phil. Soc.* **66**, 443-468.
- Burridge, R. and G. S. Halliday (1971). Dynamic shear cracks with friction as models for shallow focus earthquakes, *Geophys. J.* **25**, 261-283.
- Burridge, R. and C. Levy (1974). Self-similar circular shear cracks lacking cohesion, *Bull. Seism. Soc. Am.* **64**, 1789-1808.
- Cherry, J. T., E. J. Halda, and K. G. Hamilton (1976). A deterministic approach to the prediction of free field ground motion and response spectra from stick-slip earthquakes, *Earthquake Eng. Struct. Dyn.* **4**, 315-332.
- Dahlen, F. A. (1974). On the ratio of P-wave to S-wave corner frequencies for shallow earthquake sources, *Bull. Seism. Soc. Am.* **64**, 1159-1180.
- Das, S. and K. Aki (1977). A numerical study of two-dimensional spontaneous rupture propagation, *Geophys. J.* **50**, 643-668.
- Day, S. M. (1977). Finite element analysis of seismic scattering problems, *Ph.D. dissertation*, University of California, San Diego.

- Dieterich, J. H. (1973). A deterministic near-field source model, *Proc. World Conf. Earthquake Eng., 5th, Paper 301*.
- Eshelby, J. D. (1957). The determination of the elastic field of an ellipsoidal inclusion, and related problems, *Proc. Roy. Soc. London* **241**, 376-396.
- Eshelby, J. D. (1969). The elastic field of a crack extending non-uniformly under general anti-plane loading, *J. Mech. Phys. Solids* **17**, 177-199.
- Frazier, G. A. and C. M. Petersen (1974). 3-D stress wave code for the Illiac IV, *Systems, Science and Software Report SSS-R-74-2103*.
- Freund, L. B. (1972). Energy flux into a tip of an extending crack in an elastic solid, *J. Elasticity* **2**, 341-349.
- Fuchs, K. and G. Müller (1971). Computation of synthetic seismograms with the reflectivity method and comparison with observations, *Geophys. J.* **23**, 417-433.
- Griffith, A. A. (1921). The phenomena of rupture and flow in solids, *Phil. Trans. Roy. Soc. London, Ser. A*, **221**, 163-198.
- Hanson, M. E., A. R. Sanford, and R. J. Shaffer (1974). A source function for a dynamic brittle unilateral shear fracture, *Geophys. J.* **38**, 365-376.
- Haskell, N. A. (1964). Total energy and energy spectral density of elastic wave radiation from propagating faults, *Bull. Seism. Soc. Am.* **54**, 1811-1841.
- Haskell, N. A. (1969). Elastic displacements in the near-field of a propagating fault, *Bull. Seism. Soc. Am.* **59**, 865-908.
- Hussein, M. I., Jovanovich, D. B., Randall, M. J., and Freund, L. B. (1975). The fracture energy of earthquakes, *Geophys. J.* **45**, 367-385.
- Ida, Y. (1972). Cohesive force across the tip of a longitudinal-shear crack and Griffith's specific surface energy, *J. Geophys. Res.* **77**, 3796-3805.
- Keilis-Borok, V. I. (1959). On estimation of the displacement in an earthquake source and of source dimensions, *Ann. Geofis. (Rome)* **12**, 205-214.
- Kostrov, B. V. (1964). Self-similar problems of propagation of shear cracks, *J. Appl. Math. Mech.* **28**, 1077-1087.
- Kostrov, B. V. (1966). Unsteady propagation of longitudinal shear cracks, *J. Appl. Math. Mech.* **30**, 1241-1248.
- Kostrov, B. V. (1970). The theory for the focus for tectonic earthquakes, *IZV., Earth Phys.* **4**, 258-267.
- Kostrov, B. V. (1974). Crack propagation of variable velocity, *J. Appl. Math. Mech.* **38**, 511-519.
- Madariaga, R. (1976). Dynamics of an expanding circular fault, *Bull. Seism. Soc. Am.* **66**, 639-666.
- Neuber, H. (1937). *Kerbspannungslehre*, Springer-Verlag, Berlin; theory of notch stresses: Principles for exact calculation of strength with reference to structural form and material, The Office of Tech. Info., AEC-tr-4547, 1958 (English translation).
- Reid, H. F. (1910). Mechanics of the earthquake, in *The California Earthquake of April 18, 1906, II*: Carnegie Inst. of Washington D. C. (updated in 1969).
- Richards, P. G. (1973). The dynamic field of a growing plane elliptical shear crack, *Intern. J. Solids Struct.* **9**, 843-861.
- Richards, P. G. (1976). Dynamic motions near an earthquake fault: A three-dimensional solution, *Bull. Seism. Soc. Am.* **66**, 1-32.
- Savage, J. C. (1966). Radiation from a realistic model of faulting, *Bull. Seism. Soc. Am.* **56**, 577-592.
- Savage, J. C. and M. D. Wood (1971). The relation between apparent stress and stress drop, *Bull. Seism. Soc. Am.* **61**, 1381-1388.
- Smith, W. (1974). The application of finite element analysis to body wave propagation problems, *Geophys. J.* **42**, 747-768.
- Stöckl, H. (1977). Finite difference calculation of stress relaxation earthquake models, *J. Geophys.* **43**, 311-327.
- Trifunac, M. D. and F. E. Udawadia (1974). Parkfield, California, earthquake of June 27, 1966: A three-dimensional moving dislocation, *Bull. Seism. Soc. Am.* **64**, 511-533.

INSTITUTE OF GEOPHYSICS AND PLANETARY PHYSICS
 SCRIPPS INSTITUTION OF OCEANOGRAPHY
 UNIVERSITY OF CALIFORNIA, SAN DIEGO
 LA JOLLA, CALIFORNIA 92093

Manuscript received August 29, 1977